Statistical Downscaling of Satellite Imagery to Predict Above Ground Biomass of Cotton (*Gossypium hirsutum L.*)

by

Joseph Franklin Powell

(Under the Direction of Lynne Seymour)

Abstract

Remotely sensed satellite data provide essential monitoring of Earth's ecosystems continuously through time to supplement field level studies. The implementation of uncrewed aerial system (UAS) imagery collection to study agricultural trends in ecological research studies has fueled interest in techniques to bridge spatial scales between remotely sensed images to drive more effective land management. How to combine spatially and temporally incompatible data remains an ongoing effort. This dissertation studies the connections between multispectral imagery at different scales by gauging the effectiveness of two statistical downscaling approaches motivated by climate downscaling: regression kriging (RK) and artificial augmentation (AA). While these statistical downscaling approaches typically make predictions at a discrete number of ground surface points, we propose adaptations of the methods to construct a grid of predictions by treating each UAS pixel as a spatial site. RK makes use of variograms as part of the spatial prediction process, so we employ Spherical and Matérn variograms when constructing our downscaling

models. We form two novel sets of statistical downscaling predictions by combining the RK and AA procedures (RKAA and Joint). We implement these downscaling techniques to translate Normalized Difference Vegetation Index (NDVI) values from the planetary to the field scale. We also incorporate field level measurements of above ground biomass of cotton (*Gossypium hirsutum L.*) crops collected from the United States Department of Agriculture (USDA) study site in Ashburn, GA. The above ground biomass data is collected at six sampling plots across the study site. We construct linear regression models to predict above ground biomass as a function of each downscaled predictor in order to extrapolate the above ground biomass data from the six sampling plots to the entire study site. We assess the downscaled predictions by comparing them to ground truth predictions created from UAS data. The AA predictions show the highest accuracy, followed by the RKAA and Joint predictions. The RK predictions are significantly hindered by the concentrated sampling of the field level data, but have the capacity for improvement with additional modifications. Simulation study results show similar performance among the downscaled predictors.

INDEX WORDS: Statistical Downscaling, Regression Kriging, Spatial Prediction, Remote Sensing, Regionalization

Statistical Downscaling of Satellite Imagery to Predict Above Ground Biomass of Cotton (*Gossypium hirsutum L.*)

by

Joseph Franklin Powell

A.B., University of Georgia, 2015

B.S., University of Georgia, 2015

M.A.S., Georgia State University, 2017

M.S., Georgia State University, 2017

A Dissertation Submitted to the Graduate Faculty of the

University of Georgia in Partial Fulfillment of the Requirements for the Degree.

Doctor of Philosophy

Athens, Georgia

2024

Statistical Downscaling of Satellite Imagery to Predict Above Ground Biomass of Cotton (*Gossypium hirsutum L.*)

by

Joseph Franklin Powell

Major Professor: Lynne Seymour

Committee: Alisa Coffin

Marguerite Madden

Jaxk Reeves

Electronic Version Approved:

Ron Walcott

Dean of the Graduate School

The University of Georgia

August 2024

Acknowledgments

I must begin by acknowledging and thanking the USDA-ARS, SEWRL, and LTAR Network researchers for funding and data collection. This project was supported by the Gulf Atlantic Long-Term Agroecosystem Research (LTAR) site (cooperative agreement with Marguerite Madden and Lynne Seymour grant contracts # 58-6048-7-036 and #58-6048-2-012). We thank Coby Smith and numerous student workers for their help in the field and laboratory. We especially thank the Williford family and Mr. Todd Barnett for use of the fields.

I would like to thank my advisor, Dr. Lynne Seymour, and my committee members, Dr. Alisa Coffin, Dr. Marguerite Madden, Dr. Jaxk Reeves, and Dr. Jeongyoun Ahn, for their valuable advice, encouragement, and dedication.

I would also like to thank all of the students I have personally worked with on this project. This work has been a significant deviation from typical statistical studies, so I truly appreciate the incredible collaboration of this team: Austin Stone, Marley Holder, Kyle Steen, and Zhenyi Lei.

I would not be here without a few individuals gently nudging me on my journey. First, a great deal of thanks to Jeff Lalaian for igniting my passion for statistics. Next, thanks to Jorge Vallejos for encouraging my pursuit of a PhD. Finally, thanks to Hunter Miller and Dr. Subham Das, the other members of

Dr. Kim Gilbert's "three musketeers", without whom I never would have survived the grind of PhD coursework.

Last but not least, I would like to express my sincere thanks and gratitude to my family for their support and encouragement through twenty-seven consecutive years of education. Mom and Dad, not once did you ever question any decision I made with my studies. You two have provided for me time and time again, and I am so thankful for your generosity and love. Finally, to my wife, thank you for going through the trials of PhD life alongside me. And I'm thankful that you finally stopped asking when I would be done.

Contents

Acknowledgments **iv**

List of Figures **viii**

List of Tables **xii**

1 Introduction **1**

1.1 Literature Review 5

1.2 Multispectral Imagery and Ground Level Data 8

2 Methodology **28**

2.1 Regression Kriging 32

2.2 Artificial Augmentation 36

2.3 Simulation 40

3 Analysis **51**

3.1 Regression Kriging 51

3.2 Artificial Augmentation 55

3.3 Biomass Predictions 59

4 Conclusion and Future Directions **62**

Bibliography **67**

Appendix A **76**

List of Figures

1.1 USDA LTAR Network [Source: USDA-ARS (2022)] 2

1.2 GACP region, part of the USDA LTAR network [Source: Stone (2023)] 3

1.3 Examples of upscaling and downscaling [Source: Markham et al. (2022)] 4

1.4 Coarse-scale resolution's effect on detecting spatial detail [Source: Pan Geography (2022)] 5

1.5 Regression kriging illustration using a cross-section of the spatial field [Source: Hengl (2009)] 8

1.6 Ashburn farm 9

1.7 GACP region and HUC watershed boundaries 10

1.8 Wavelengths of the 5-band MicaSense RedEdge multispectral sensor [Source: AgEagle Aerial Systems Inc. (2024)] 12

1.9 An illustration of a multilayer image consisting of five component layers or bands. [Source: Liew (2001)] 13

1.10 5-band (1. blue, 2. green, 3. red, 4. red-edge, 5. near-infrared) UAS spectral reflectance comparison between sampling plots in cotton (Sample 39) and peanut (Sample 36) fields [Source: Stone (2023)] 13

1.11 Wavelengths of the Landsat and Sentinel multispectral sensors [Source: USGS EROS (2019)] 15
1.12 Upscaled 9 cm pixels of UAS imagery of the ACF to 10 m Sentinel-2 MSI satellite image and 30 m Landsat 8 OLI satellite image pixel sizes [Source: Stone (2023)] 16
1.13 Tree Structure for Multiscale Processes 18
1.14 Six sampling plots (30 m by 10 crop row rectangles) chosen for intensive sampling throughout the growing season; sample locations indicated by yellow rectangles [Source: Stone (2023)] 21
1.15 Field sampling scheme used for collecting ground level data at the intensive sampling plots. Each of the ten sampling plot crop rows was subdivided into 1 m sections, with ten 1 m sections sampled during each sampling period as indicated by the sampling date numbers in the green boxes. For example, all of green boxes labeled '1' were sampled on the first collection date, followed by all of the green boxes labeled '2' on the second collection date, and so on. Rows 2, 3, 8, and 9 were never sampled because those rows were used at each visit to capture digital hemispherical photographs. [Source: Coffin et al. (2024)] 22
1.16 Above ground biomass dry weight measurements across the sampling dates for each sampling plot (SampleID) 23
1.17 Temporal changes in NDVI, EVI2, and SAVI at each of the six intensive sampling plot areas 24
1.18 Temporal changes in NDVI and above ground biomass at each of the six intensive sampling plot areas 25

1.19 Comparison of NDVI values captured by UAS, Sentinel, and Landsat imagery. Error bars show 95% confidence intervals. 27

2.1 The sill, nugget, and range define the behavior of the variogram. [Source: Biswas and Si (2013)] 34

2.2 The regression kriging predictor possesses a starburst visual effect as the predictions were extrapolated from the sampling plots 37

2.3 Workflow implemented to create a weighted biomass raster from the single biomass sample and the UAS measured NDVI over the 30 m x 10 row biomass sampling plot. Biomass data are publicly available in Ag Data Commons (Coffin et al., 2023). [Source: Stone (2023)] 41

2.4 Illustration of the different simulated resolutions 44

2.5 Simulation sampling scheme: all response variable data and explanatory variable data was collected from the shaded areas. 45

2.6 Simulation sample variogram with fitted Spherical and Matérn variogram curves 45

2.7 Four simulated downscaled predictors from satellite level data 46

2.8 Simulated ground level biomass predictions (in g/pixel) from the four predictors 47

2.9 Predicted biomass from simulated UAS level data 49

2.10 Mean squared error violinplots from 100 simulations, with boxplots inside the violin areas. 50

3.1 ACF Sentinel pixel polygons after edge pixel and 'no data' pixel removal, with the original field boundary shown in green. 52

3.2 Sample variograms with the fitted lines for Spherical and Matérn variogram models. . . 54

3.3 The regression kriging predictor possesses a starburst visual effect as the predictions were extrapolated from the sampling plots 56

3.4 Four statistical downscaling predictors formed from Sentinel and UAS NDVI values. . 58

3.5 Biomass prediction plots (in g/pixel) from the five predictors. 61

A.1 Sample variogram from the failed seed. 77

A.2 Simulated X_1, X_2, and ϵ from the failed seed. 77

A.3 Simulated UAS level and ground level response variables from the failed seed. 78

List of Tables

1.1 Spectral reflectance bandwidths (in nm) of UAS, Sentinel, and Landsat imagery 12

1.2 Date groupings of UAS, Sentinel, and Landsat imagery 14

2.1 Mean squared error statistics from 100 simulations 49

3.1 Variogram parameter estimates for the upper and lower field models. 54

3.2 Workflow of the artificial augmentation reweighting process applied to UAS and Sentinel NDVI values. 57

3.3 Mean squared error and bias statistics from four downscaled predictors measured against the UAS imagery. 59

3.4 Mean squared error statistics from five biomass predictors. 60

Chapter 1

Introduction

Studying long-term agricultural trends is crucial for understanding the future of food security and agricultural production in response to increasing global population, climatic variations, and economic demand. The United States Department of Agriculture Agricultural Research Service (USDA-ARS) currently operates the Long-Term Agroecosystem Research (LTAR; USDA-ARS, 2022) Network to research solutions for resilient, climate-smart agriculture in the conterminous United States (Figure 1.1). The network includes the Gulf Atlantic Coastal Plain (GACP) LTAR site, a region spanning across South Georgia and into both Florida and South Carolina within the Southeastern Plains ecoregion (Figure 1.2). The GACP region is managed by the ARS Southeast Watershed Research Laboratory (SEWRL) in Tifton, GA, where scientists have been observing hydrologic systems in the 334 km^2 Little River Experimental Watershed (LREW) since the late 1960s, climatic systems since the 1970s, and cropping and land use systems since the early 2000s (USDA-ARS, 2024).

The LTAR Network is interested in understanding the characteristics that define the GACP site and other LTAR sites to define their regions (Bean et al., 2021; Kumar et al., 2023). By determining regions of

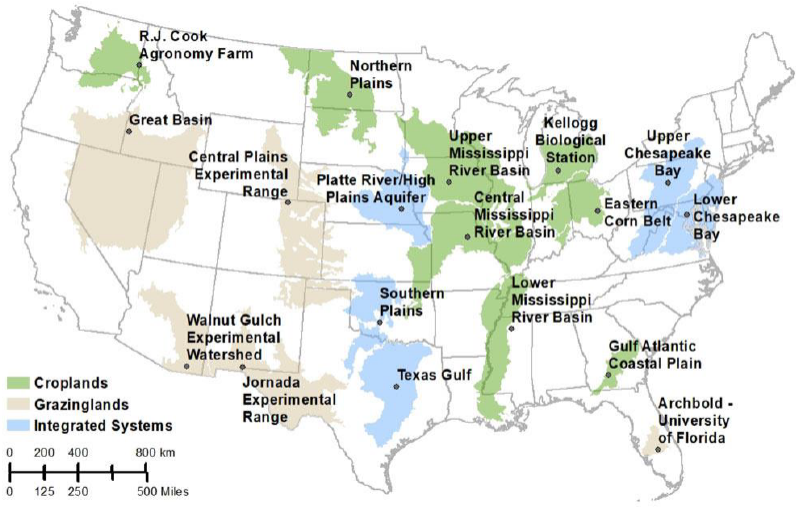

Figure 1.1: USDA LTAR Network [Source: USDA-ARS (2022)]

similarity, the LTAR Network can perform localized experiments, analyze the results of the experiments, and infer similar results across the region. This regionalization task requires bridging the scaling gap (both upscaling and downscaling) between field-level observations and remotely sensed observations, such as uncrewed aerial system (UAS) and satellite (e.g., Sentinel-2 and Landsat 8) imagery (Yin et al., 2018; Zappa et al., 2019). Upscaling converts image data collected at a finer resolution to a coarser resolution, often via some summarizing approach such as averaging; downscaling takes the opposite approach, allocating coarser data to a finer scale, usually by estimating the spatial distribution of values in the image (Markham et al., 2022). The simplest form of downscaling is downsampling (or resampling), a process by which the larger image pixel is subdivided into smaller pixels and the value of the large pixel is assigned to each of the smaller pixels. Examples of both an upscaling process via averaging and a downscaling process via downsampling are shown in Figure 1.3.

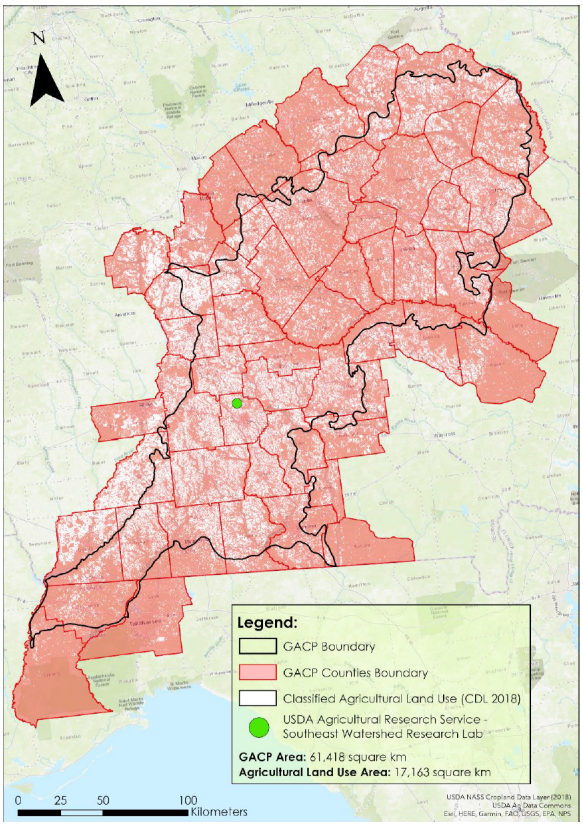

Figure 1.2: GACP region, part of the USDA LTAR network [Source: Stone (2023)]

Small fields (i.e., < 5 ha) are prevalent within the GACP LTAR site (Coffin et al., 2022). Their small size and variable dimensions lead to errors in crop classification datasets that use satellite reflectance data with resolutions of 30 m pixels or larger (e.g., Landsat). Also, farm-to-farm crop diversity is high in the LREW region. Moderate-scale satellite imagery, such as Landsat with 30 m resolution, is insufficient to properly analyze these types of fields. The effect resolution plays in detecting spatial detail on the land surface can be seen in Figure 1.4, with coarser resolution failing to identify the variety of land cover categories while finer resolution can pick up details about land cover. Our multiscale research utilized the fine scale of the UAS imagery to study sub-satellite-pixel variation, which improves the link between

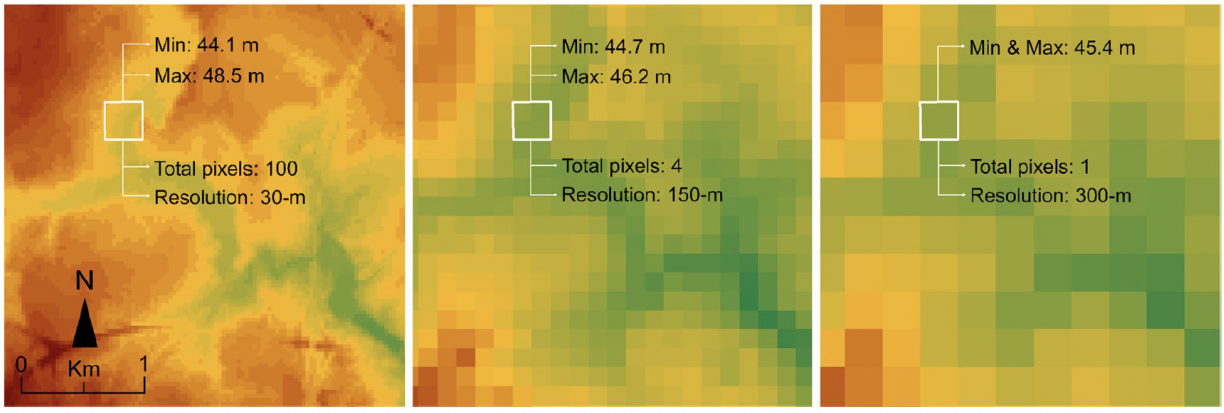

(a) Upscaling uses the mean of the input cells to construct a coarser resolution image.

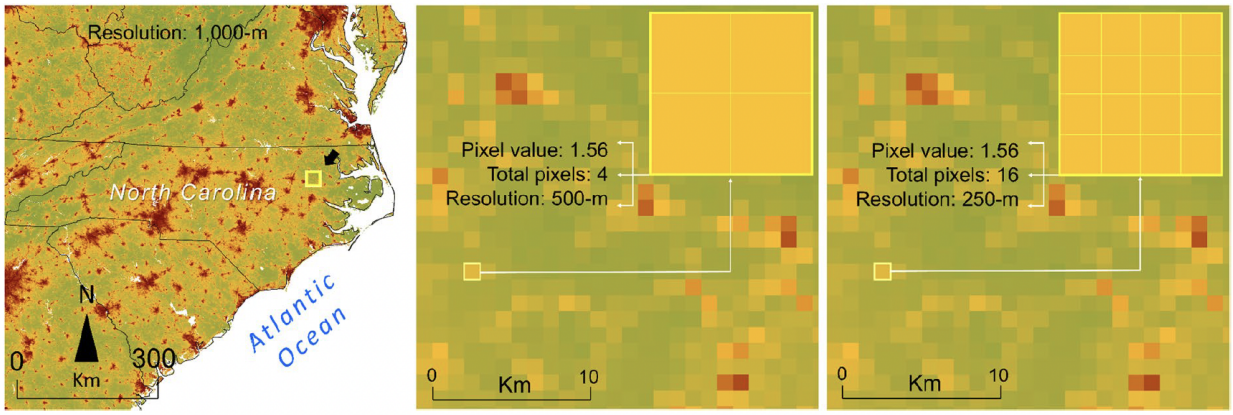

(b) Downsampling (downscaling) subdivides the coarse-scale pixel into fine-scale pixels, with each fine-scale pixel receiving the original value of the coarse-scale pixel.

Figure 1.3: Examples of upscaling and downscaling [Source: Markham et al. (2022)]

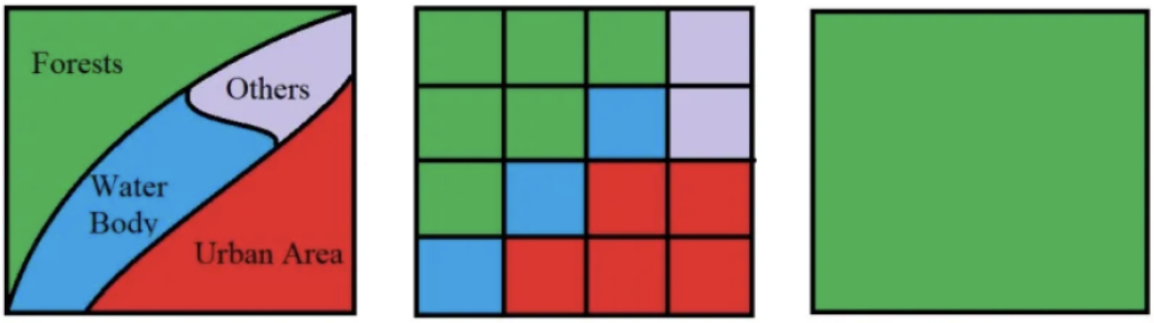

(a) Land Surface

(b) Satellite Imagery
1 pixel = 250 m^2

(c) Satellite Imagery
1 pixel = 1 km^2

Figure 1.4: Coarse-scale resolution's effect on detecting spatial detail [Source: Pan Geography (2022)]

satellite imagery and the land surface Powell et al. (2022); Stone (2023). Our objective was to produce a prediction model for the above ground biomass of cotton (*Gossypium hirsutum L.*) using a combination of satellite imagery, UAS imagery, and ground level data.

1.1 Literature Review

Extrapolation of ecological data is often nontrivial. Miller et al. (2004) highlighted the typical procedures and pitfalls involved in spatial extrapolation to broader scales or new locations. Predicting ground level ecological data from satellite imagery yields an additional set of challenges based on scale (Gahrouei et al., 2020). Gotway and Young (2002, 2007) outlined a theoretical methodology for linking these incompatible measurements, which may differ in scale, resolution, dimension, etc. Markham et al. (2022) reviewed current upscaling and downscaling methods, characterizing them based on ease of implementation. Revill et al. (2020) also studied the uncertainty of the scaling gap in terms of measuring leaf area index between satellite and UAS imagery.

The use of UAS imagery collection for ecological research studies has fueled the development of techniques to bridge spatial scales between remotely sensed images. Machine learning and deep learning analysis are increasingly commonplace in remote sensing. Machine learning is a form of artificial intelligence concerned with computer algorithms that use data to extract solutions to often complex, nontrivial problems. Deep learning is a type of machine learning which uses a neural network (sequence of layers comprised of nodes and connections) to dissect the input data and produce predictions (LeCun et al., 2015). Deep learning is praised for its flexibility in the types of data that can be studied, including images and videos. Markham et al. (2022) categorized general machine learning techniques as moderately complex downscaling methodologies to implement, while deep learning was labelled as a highly complex downscaling approach.

Data fusion is a remote sensing technique used to combine characteristics of multiple data sources (Sohn and Dowman, 2007; Dong et al., 2009; Zhang, 2010). For example, high-frequency temporal information from one source can be blended with high-resolution spatial information from another source to produce synthetic data that are both high-frequency and high-resolution. Gao et al. (2006) combined finer resolution Landsat surface reflectance imagery, that has a 16-day revisit cycle, with coarser Moderate Resolution Imaging Spectroradiometer (MODIS) daily surface reflectance to construct synthetic "daily" Landsat surface reflectance data. Gao et al. (2017) applied this approach to mapping crop phenology using vegetation index data generated by Landsat-MODIS fusion.

Many studies in remote sensing focus on image classification, land use and land cover, or predicting some measure of vegetation (e.g., crop biomass, leaf area index, vegetation index; Gahrouei et al., 2020; Revill et al., 2020; Scott et al., 2017; Zhang et al., 2021). The methods used for these types of analysis include support vector machines (SVMs; Boser et al., 1992; Guo et al., 2008, 2018; Pal, 2009) and a type of

deep learning called convolutional neural networks (CNNs; Farabet et al., 2013; Hamdi et al., 2019; Kussul et al., 2017). The SVMs are popular machine learning algorithms used for classification. They operate by forming a separating boundary between two classes (in a 2-dimensional setting, this would be a line separating points in a scatterplot; in higher dimensions, the boundary becomes a hyperplane). In order to maximize the SVM's ability to correctly classify, the separating hyperplane is selected to maximize the margin, or distance, between the hyperplane and the nearest observations of either class. These observations which define the maximum margin are called support vectors. The SVM classification solution is represented as a linear combination of the support vectors. The CNNs are often used in image analysis due to their ability to learn spatial features and patterns. As the name implies, a CNN convolves a kernel matrix with the input matrix representing an image. For each pixel in the image, the kernel matrix also operates on the pixel's neighbors during the convolution. The sourcing of information from neighboring pixels is what drives the CNN to learn spatial features and patterns.

In geostatistics, kriging is one of the primary means of quantifying spatial correlation patterns between data locations (Cressie, 1993; Matheron, 1963). Simple (or ordinary) kriging interpolates point observations of the target variable in order to form weighted-average predictions at sites without observations. Another strategy, called universal kriging, involves interpolation using a regression equation to form predictions based on auxiliary variables, such as the coordinates of the observation locations (Matheron, 1969). Recently, there has been a surge in the use of hybrid techniques involving a combination of simple and universal kriging techniques (Hengl et al., 2007). One such hybrid approach is regression kriging (RK; Hengl et al., 2004, 2007; Odeh et al., 1995), which forms predictions by first using regression on auxiliary variables and then using simple kriging to interpolate the regression residuals. Hengl et al. (2007) proved that universal kriging and RK produce the same predictions and prediction variances despite their

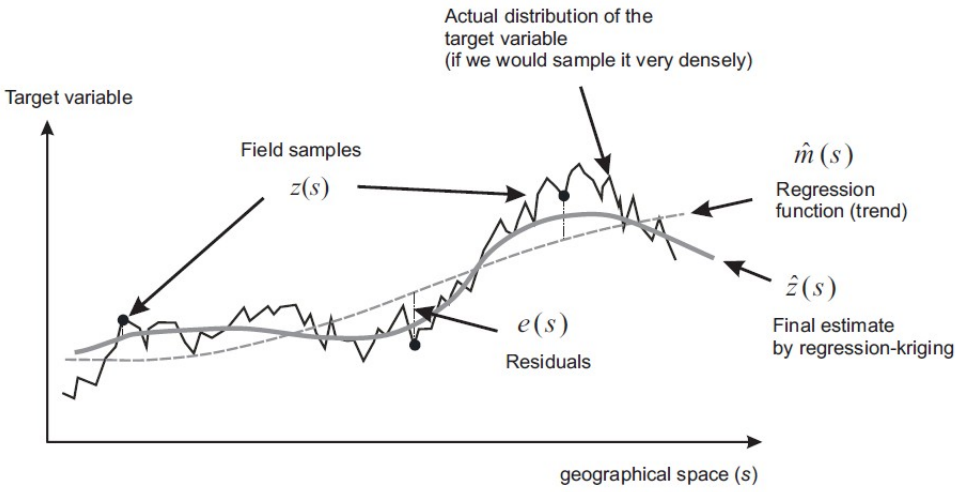

Figure 1.5: Regression kriging illustration using a cross-section of the spatial field [Source: Hengl (2009)]

differing computational steps. However, RK has the advantage of separating the regression estimation and residual interpolation steps, allowing for arbitrarily complex forms of regression compared to the limited linear regression techniques that can be utilized in universal kriging. Additionally, this separation approach in RK allows both components to be interpreted individually. RK fits the overall trend of the target variable before adjusting for the residuals (Figure 1.5). RK has been introduced in remote sensing and agricultural studies as a moderately complex downscaling method (Markham et al., 2022). Jin et al. (2018) used RK to downscale surface soil moisture, while Mukherjee et al. (2015) used this approach to downscale land surface temperature.

1.2 Multispectral Imagery and Ground Level Data

Before attempting to analyze the GACP region as a whole, we centered our attention on our initial study area of the Ashburn Cooperator Farm (ACF; 31°42′24″N, 83°43′35″W). The USDA-ARS in Tifton, GA,

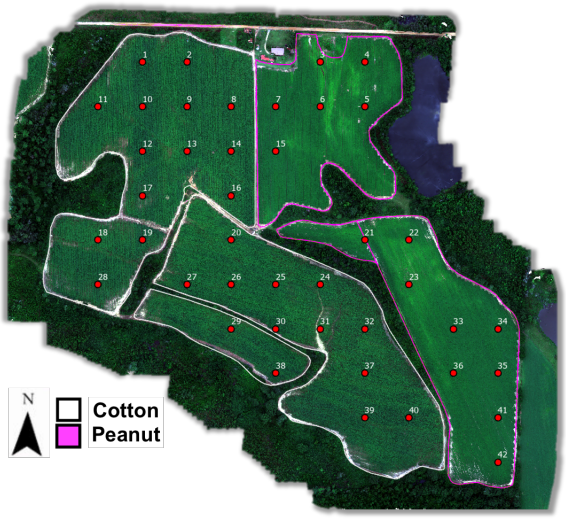

Figure 1.6: Ashburn farm - In 2018, cotton was planted in the western fields outlined in white and peanuts were planted in the eastern fields outlined in fuchsia. The red numbered dots are field-level sampling points. [Source: Stone (2023)]

has been conducting research here since 2014, collecting field measurements of crops and soil throughout the year. Acquisition of UAS imagery at the site began in 2017. During 2018, the farm grew cotton in the western fields and peanuts in the eastern fields (Figure 1.6). The multiscale focus in the regionalization effort is illustrated in Figure 1.7, comparing the sampling plot to the boundary of the ACF study site to the boundaries of the Hydrologic Unit Code (HUC) watersheds and to the boundary of the GACP region.

Seasonal UAS imagery acquired by the USDA-ARS SEWRL records the growth of crops (e.g., corn, cotton, and peanuts) at 9 cm pixel resolution using a 5-band MicaSense RedEdge multispectral sensor (blue, green, red, red-edge, near-infrared (NIR); Figure 1.8 and Table 1.1) mounted on a DJI Matrice quadcopter (M100 in 2018 and M210RTK in 2019). Each band of the multispectral sensor forms a layer of the image (i.e., image band) while still capturing the same spatial extent of the ground surface (Figure 1.9). We also computed vegetation indices based on ratios of these spectral reflectance values. Specifically,

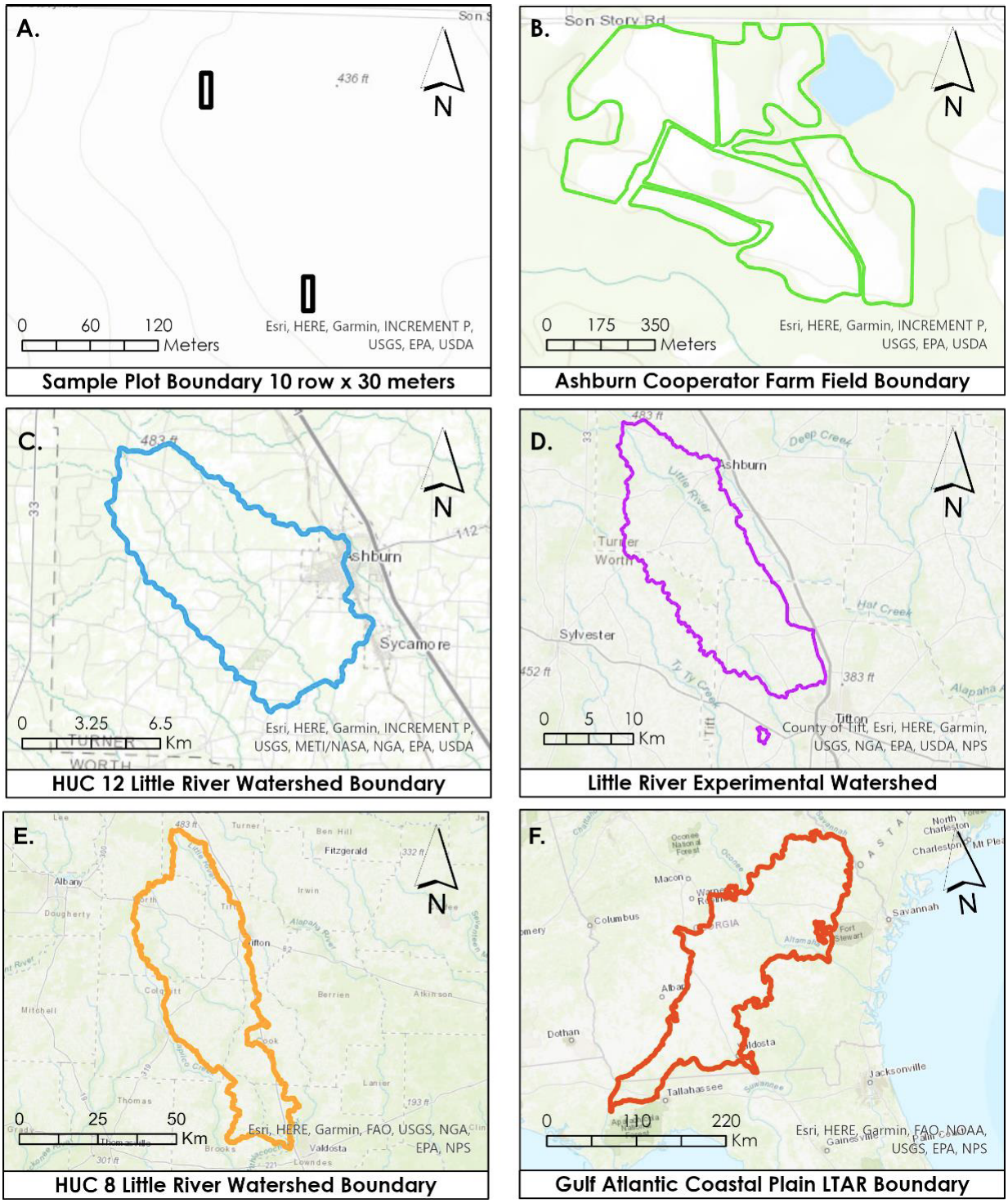

Figure 1.7: Regionalization involves taking measurements within the A.) rectangular sampling plot boundaries and extrapolating to the B.) field, to the Little River Watershed C.) HUC 12, D.) HUC 10, and E.) HUC 8, and to the F.) GACP region. [Source: Stone (2023)]

we considered the Normalized Difference Vegetation Index (NDVI; Tucker, 1978), the 2-band Enhanced Vegetation Index (EVI2; Jensen, 2000), and the Soil-Adjusted Vegetation Index (SAVI; Heute, 1988) of the crops as registered by the UAS sensor. The NDVI, a common measure of vegetation health, is given by:

$$NDVI = \frac{NIR - Red}{NIR + Red}, \tag{1.1}$$

where NIR is the near-infrared spectral reflectance value and Red is the red spectral reflectance value. The EVI2, a measure with improved sensitivity to vegetation with high biomass, is produced by:

$$EVI2 = 2.5 \cdot \left(\frac{NIR - Red}{NIR + 2.4 \cdot Red + 1} \right). \tag{1.2}$$

The SAVI, a measure that adjusts for the considerable amount of soil visible during the early stages of the growing season, is calculated as:

$$SAVI = \left(\frac{(1 + L)(NIR - Red)}{NIR + Red + L} \right), \tag{1.3}$$

where L is a canopy background adjustment factor that is approximated as 0.5 to reduce soil brightness variations. Multispectral measurements with the UAS were collected across 8 dates between June and October of 2018: June 18, July 11 and 24, August 3 and 31, September 7 and 21, and October 17. The UAS imagery of the 111 acre farm was captured at nadir (directly beneath the UAS sensor at 120 m altitude) and required about 300 images per flight to cover the study area growing both cotton and peanuts. An example of spectral reflectance changes across three measurement dates for both cotton and

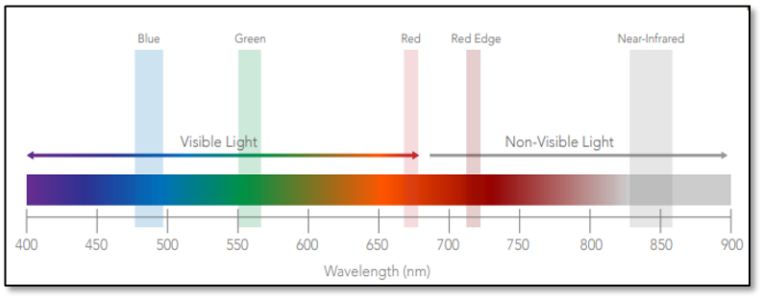

Figure 1.8: Wavelengths of the 5-band MicaSense RedEdge multispectral sensor [Source: AgEagle Aerial Systems Inc. (2024)]

Table 1.1: Spectral reflectance bandwidths (in nm) of UAS, Sentinel, and Landsat imagery

Band	UAS	Sentinel	Landsat
Blue	475 ± 32	493 ± 65	480 ± 30
Green	560 ± 27	560 ± 35	560 ± 30
Red	668 ± 14	665 ± 30	655 ± 15
Red-edge	717 ± 12	–	–
NIR	842 ± 57	833 ± 104	865 ± 15

peanut sampling plots is given in Figure 1.10, showing the drop off in spectral reflectance values as the crops near harvest time.

We also utilized satellite imagery from the U.S. Landsat 8 Operational Land Imager (OLI) and European Space Agency (ESA) Copernicus Program's Sentinel-2A/2B Multi-Spectral Instrument (MSI; tile 17SKR), both of which captured blue, green, red, and near-infrared spectral reflectance (among others; USGS EROS, 2019). The various wavelength bands captured by the Landsat and Sentinel multispectral sensors are illustrated in Figure 1.11. We paid particular attention to the visible blue, green, and red bands and the NIR band (bands 2, 3, 4, and 5 for Landsat 8; bands 2, 3, 4, and 8 for Sentinel-2). Likewise with the UAS imagery, we calculated the vegetation index values produced from the satellite imagery. Landsat 8 (path/row 18/38) collected spectral reflectance imagery approximately every 16 days with a resolution of

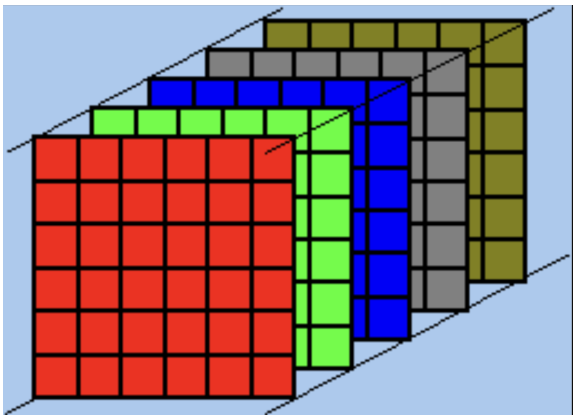

Figure 1.9: An illustration of a multilayer image consisting of five component layers or bands. [Source: Liew (2001)]

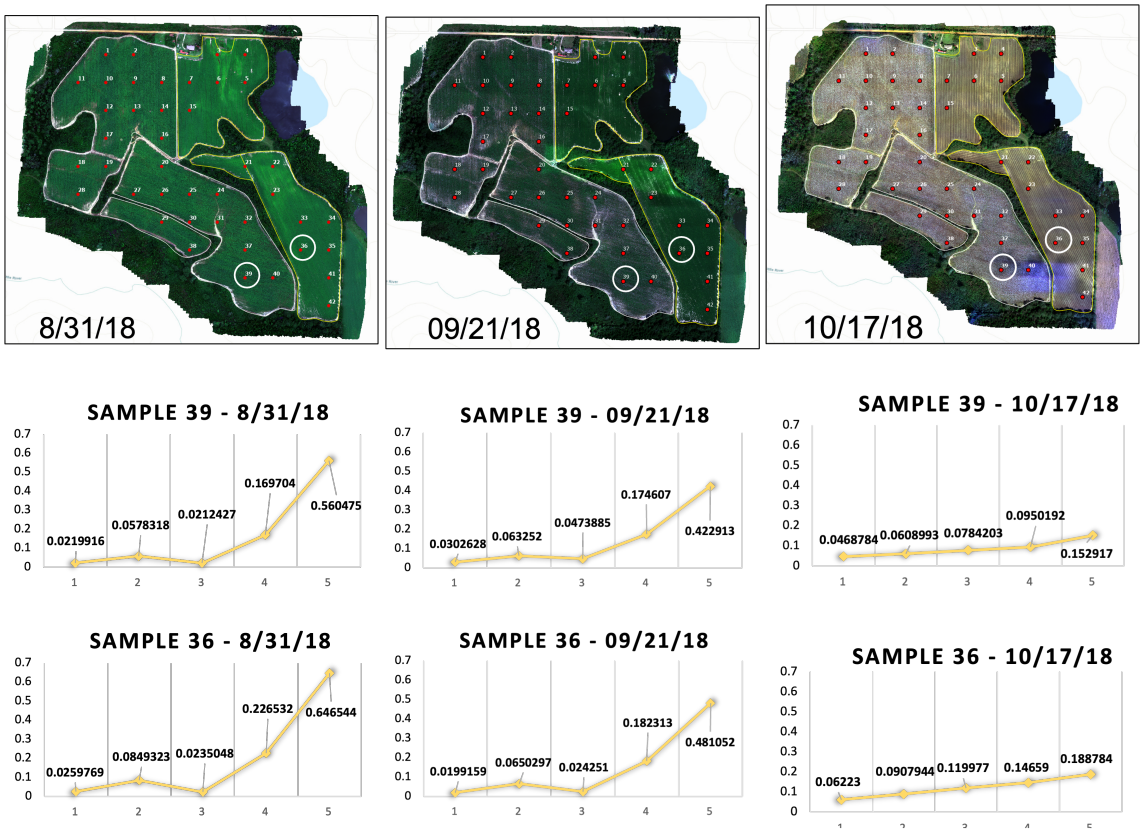

Figure 1.10: 5-band (1. blue, 2. green, 3. red, 4. red-edge, 5. near-infrared) UAS spectral reflectance comparison between sampling plots in cotton (Sample 39) and peanut (Sample 36) fields [Source: Stone (2023)]

Table 1.2: Date groupings of UAS, Sentinel, and Landsat imagery

UAS	Sentinel	Landsat
6/18	6/11	6/11
7/11	7/11	7/13
7/24	7/16	7/29
8/3	8/5	7/29
8/31	8/30	9/15
9/7	9/9	9/15
9/21	9/19	10/1
10/17	10/14	10/17

30 m ground sample distance, while Sentinel-2A/2B (tile 17SKR) passed our study area every 5 days with a ground sample distance of 10 m. Because the two satellites followed different orbits, the pixels they produced align neither spatially nor temporally. Each Landsat-level pixel overlays about $111,000$ UAS-level pixels, while each Sentinel-level pixel overlays about $12,000$ UAS-level pixels. We utilized downscaling as a means of enhancing the quantity of spectral information at our disposal while keeping the new information contained to the original ground area covered by the associated Landsat or Sentinel pixel. We collected satellite imagery for all available dates between June and October via Google Earth Engine (Gorelick et al., 2017) by writing a Python (Richert and Coelho, 2013) script which connected to Google Earth Engine and downloaded the satellite imagery for the study area. Some satellite images were abandoned because of poor image quality due to cloud cover exposure. August 2018 was a cloudy time for our study area, and nearly all of the satellite imagery during this month were discarded. For this reason, we assigned some Landsat imagery to multiple date groupings. Table 1.2 outlines the dates of the imagery we used, with each row showing how we matched up the three images into groupings for analysis.

There are certain costs associated with acquiring fine-scale imagery from the UAS sensor that currently prevent the widespread utilization of crop management using this technology. Challenges involved in

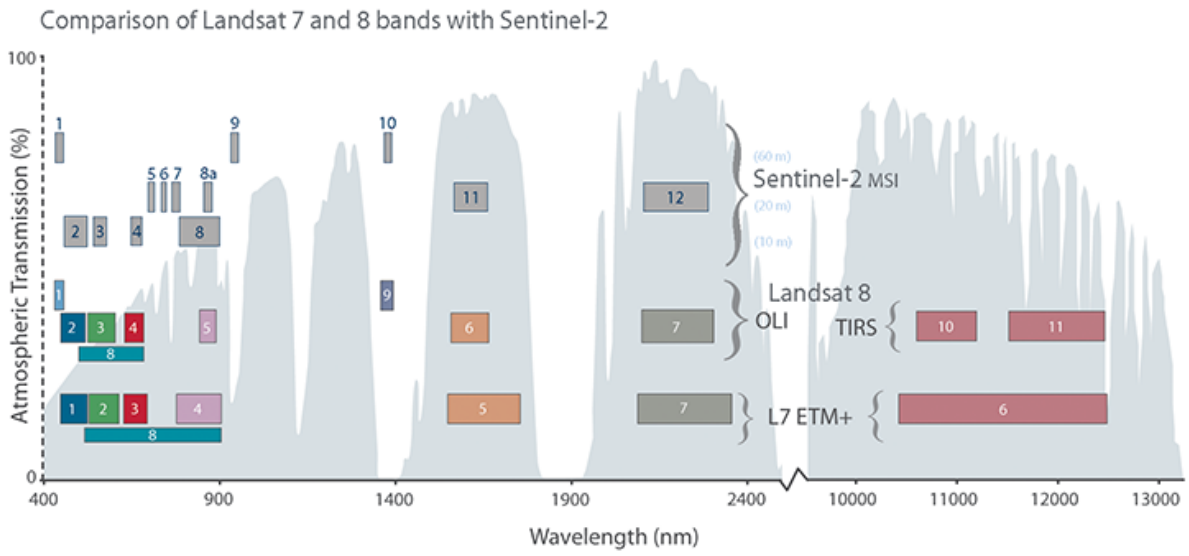

Figure 1.11: Wavelengths of the Landsat and Sentinel multispectral sensors [Source: USGS EROS (2019)]

UAS image data collection include the expense of purchasing equipment, potential for equipment failure and operator error, importance of adhering to federal and local regulations, limitations of battery life, and issues of high data volume in terms or storage, management, processing, and analysis. While satellite imagery is readily and historically available (e.g., since 1984 for 30 m Landsat 8 and since 2015 for 10 m Sentinel-2), a great deal of spatial information is lost from the coarser resolution. The loss of spatial detail in satellite imagery compared to the fine-scale resolution in the UAS imagery when upscaling is illustrated in Figure 1.12 (Markham et al., 2022). This highlights the need to include fine-scale UAS imagery in conjunction with satellite data to provide a better understanding of spatial dynamics and to inform the proper management of the crops.

In formulating our prediction model, we must understand the connection between the satellite and UAS data layers with the ground. Let us consider a generalized setting. Assume that we have an expanse

(a) 9 cm UAS (b) 10 m Sentinel-2 MSI

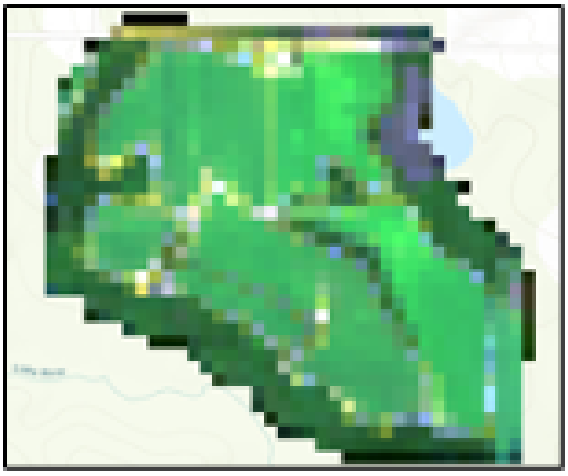

(c) 30 m Landsat 8 OLI

Figure 1.12: Upscaled 9 cm pixels of UAS imagery of the ACF to 10 m Sentinel-2 MSI satellite image and 30 m Landsat 8 OLI satellite image pixel sizes [Source: Stone (2023)]

of ground labelled A. Let the ground surface extent of a UAS pixel be A_U, the ground surface extent of a Sentinel-2 pixel be A_S, and the ground surface extent of a Landsat 8 pixel be A_L, where $A_U \subset A_S \subset A_L \subset A$. The spectral reflectance values of the satellite and UAS imagery are functions of the ground level characteristics (e.g., plants, roads, water, buildings) within their associated ground surface extents. For UAS, Sentinel-2, and Landsat 8 pixels, respectively, we define a set of transformations from ground level characteristics to spectral reflectance values $f_U, f_S,$ and f_L as:

$$\begin{aligned} Y_U &= f_U(X_U) \\ Y_S &= f_S(X_S) \\ Y_L &= f_L(X_L), \end{aligned} \tag{1.4}$$

where $Y_U, Y_S,$ and Y_L are the spectral reflectance values and $X_U \in A_U, X_S \in A_S,$ and $X_L \in A_L$ are the ground level characteristics within the respective ground surface extents. From here, we can define additional connections between the layers. The connections between the layers of differing scales is illustrated in Figure 1.13, with layers with coarser data incorporating the information from layers with finer-scale data. For example, we define the relationship from the UAS layer to the Sentinel-2 layer by the transformation function h_{SU}:

$$V_{SU} = h_{SU}(Y_U) = h_{SU} \circ f_U(X_U), \tag{1.5}$$

where V_{SU} is the spectral reflectance value at the Sentinel-2 level using the spectral reflectance data from the UAS level. For clarity, we can think of the connecting function between Sentinel-2 and UAS, V_{SU}, as a discrete step function that approximates the constant value, $s \in Y_S$, of the Sentinel-2 pixel. For example,

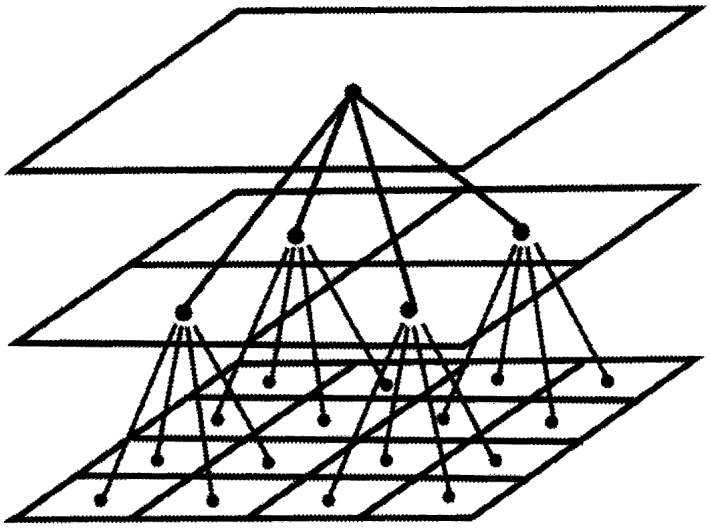

Figure 1.13: A tree structure for multiscale processes showing how the layers with coarser data aggregate the information from layers with finer-scale data. [Source: Gotway and Young (2002)]

we may have the following structure:

$$V_{SU}(y) = \begin{cases} s_1, & y_{[1]} \leq y < y_{[2]} \\ \vdots & \\ s_i, & y_{[i]} \leq y < y_{[i+1]} \\ \vdots & \\ s_{n-1}, & y_{[n-1]} \leq y \leq y_{[n]} \end{cases}, \tag{1.6}$$

where $y \in Y_U$ is the input UAS pixel value; $y_{[1]}, \ldots, y_{[i]}, \ldots, y_{[n]}$ are defined endpoints of the step function with $y_{[1]} = min(Y_U)$ and $y_{[n]} = max(Y_U)$; and $S = \{s_1, \ldots, s_i, \ldots, s_{n-1}\}$ are the step function constant values.

For our purposes, we define the downscaling relationships from Sentinel-2 and Landsat 8 to the UAS layer by transformation functions g_{US} and g_{UL}:

$$\begin{aligned} W_{US} &= g_{US}(Y_S) = g_{US} \circ f_S(X_S) \\ W_{UL} &= g_{UL}(Y_L) = g_{UL} \circ f_L(X_L), \end{aligned} \tag{1.7}$$

where W_{US} and W_{UL} are the downscaled spectral reflectance values at the UAS level using the spectral reflectance data from Sentinel-2 and Landsat 8, respectively. For clarity, we can think of the connecting function between UAS and Sentinel-2, W_{US}, as the approximate inverse of our discrete step function in Equation 1.6. The inverse function of a step function does not exist (because the step function is not a one-to-one function), but we can define an approximation of this inverse function by defining the midpoints of the intervals of UAS pixel values as the representative inverse value for each discrete step. For example, we may have the following structure:

$$W_{US}(s) = \begin{cases} \dfrac{y_{[1]} + y_{[2]}}{2}, & s_1 = \overset{\arg\inf}{t \in S} |s - t| \\ \vdots & \\ \dfrac{y_{[i]} + y_{[i+1]}}{2}, & s_i = \overset{\arg\inf}{t \in S} |s - t| \\ \vdots & \\ \dfrac{y_{[n-1]} + y_{[n]}}{2}, & s_{n-1} = \overset{\arg\inf}{t \in S} |s - t| \end{cases}, \tag{1.8}$$

where s is the input Sentinel-2 pixel value and S is the set of approximate values for s given by the function in Equation 1.6.

To include the UAS and satellite imagery in our analysis, we began with image processing to create temporal groupings of UAS and satellite images that will be analyzed as a set (Table 1.2). We first clipped

the UAS imagery using a shapefile (stores the geometric location and other attributes of geographic features, such as points, lines, and polygons) of the cotton field boundary to mask any data beyond the field boundary. Next, we reprojected, resampled, and clipped the satellite imagery to match the clipped UAS imagery in terms of coordinate reference system, pixel size, and geographic boundary, respectively. The satellite image downsampling resulted in image pixels that aligned with the UAS image pixels; however, the group of small pixels that fell within the boundary of each satellite pixel shared the same information. This process of creating fine-scale pixels from a coarse-scale pixel is illustrated in Figure 1.3 (panel b). The forthcoming Methodology section (Chapter 2) will cover a statistical downscaling approach to sharpen the spatial resolution of the satellite data.

Our final source of data came from the ground level. Six of the sampling plots shown in Figure 1.14 (plots 2, 14, 20, 28, 32, and 39) underwent intensive sampling throughout the growing season. Coffin et al. (2024) detailed the field level sampling of above ground biomass and other crop and soil information (e.g., soil moisture, plant water content, and crop height). The associated datasets are publicly available in Ag Data Commons (Coffin et al., 2023). These sampling events produced a measure of above ground biomass for each plot during each sampling period. The area of each sampling plot was 30 m by 10 crop rows, forming its own version of a ground-level pixel. The collection protocol for each sampling plot is outlined in Figure 1.15. Due to the destructive nature of plant sampling, new areas had to be sampled upon each revisit to the sampling plot. Only cotton crops were included in the intensive sampling; therefore, our study focuses solely on the cotton crop. These plots were sampled 6 times between June and October: June 18, July 12, August 3 and 31, September 21, and October 17. The above ground biomass measurements across the six sampling dates for each of the six cotton intensive sampling plot sites is shown in Figure 1.16. The biomass at all six locations steadily increased during the growing season, as expected, followed by a

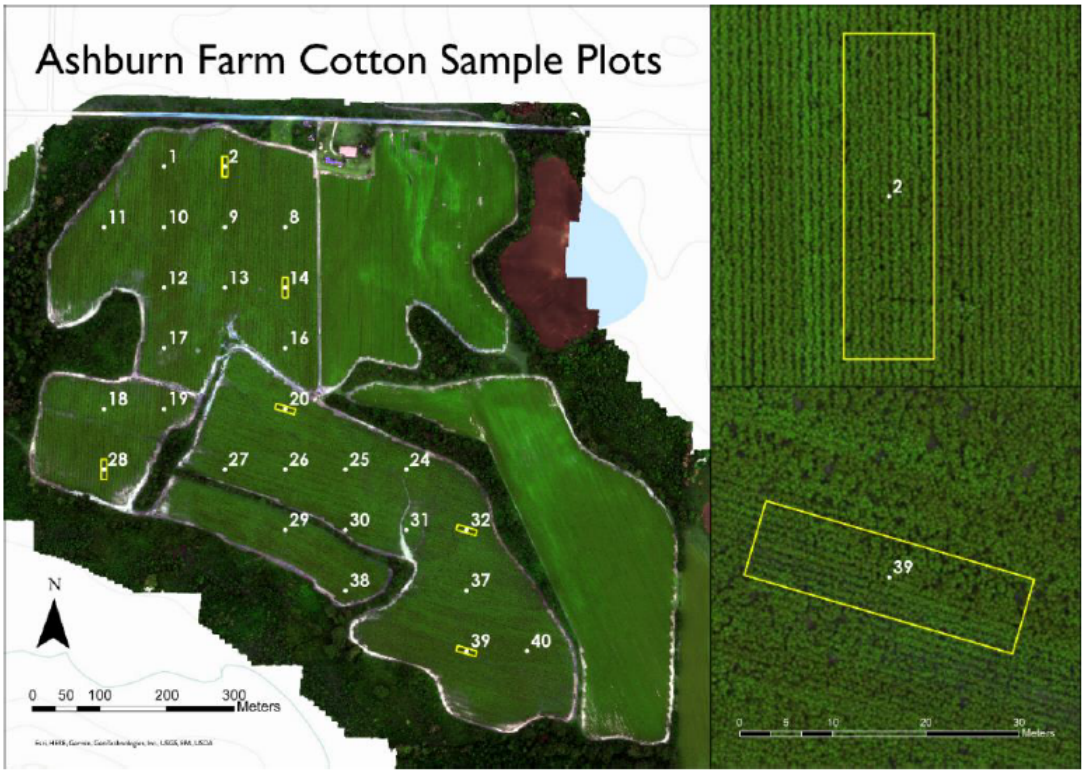

Figure 1.14: Six sampling plots (30 m by 10 crop row rectangles) chosen for intensive sampling throughout the growing season; sample locations indicated by yellow rectangles [Source: Stone (2023)]

levelling off and eventual drop off. The drop off in biomass at the last time point can be attributed to the defoliant sprayed on the cotton in preparation for harvest.

We computed NDVI, EVI2 and SAVI from the UAS 9 cm pixels contained within 42 field-level plots, 30 m by 10 crop rows in size, distributed evenly throughout the ACF cotton and peanut fields (at the red points in Figure 1.6 using the shape of the yellow rectangles in Figure 1.14). Temporal changes in computed vegetation indices from UAS pixels within the six biomass sampling plot areas (points with yellow rectangles in Figure 1.14) are compared in Figure 1.17. For each sampling plot area, we averaged the vegetation indices of the pixels within the plot boundary. Although the general shapes of the curves were

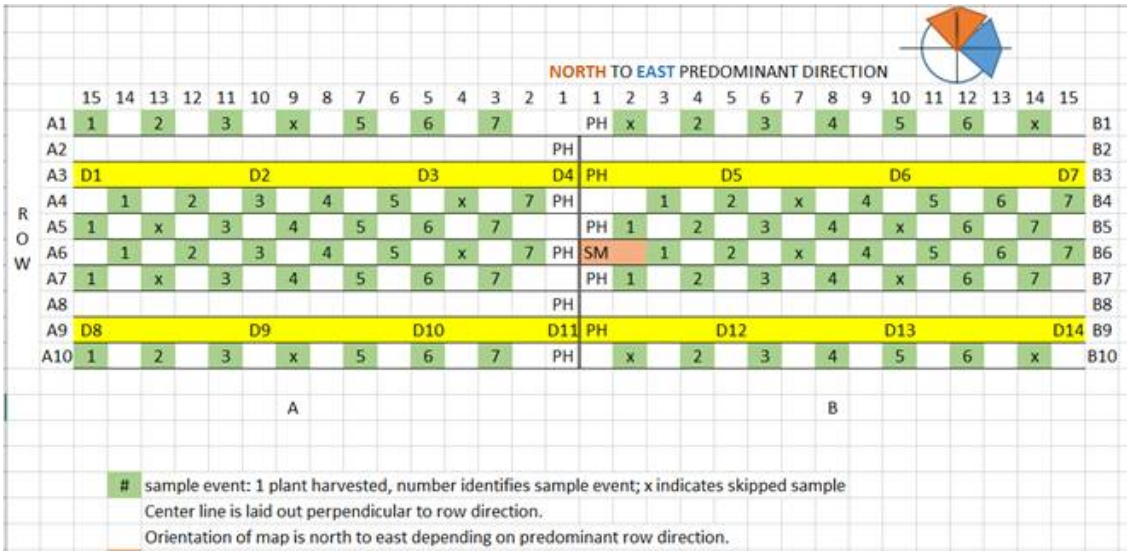

Figure 1.15: Field sampling scheme used for collecting ground level data at the intensive sampling plots. Each of the ten sampling plot crop rows was subdivided into 1 m sections, with ten 1 m sections sampled during each sampling period as indicated by the sampling date numbers in the green boxes. For example, all of green boxes labeled '1' were sampled on the first collection date, followed by all of the green boxes labeled '2' on the second collection date, and so on. Rows 2, 3, 8, and 9 were never sampled because those rows were used at each visit to capture digital hemispherical photographs. [Source: Coffin et al. (2024)]

similar for all six sampling plots, plots 14 and 28 showed a notable decrease in EVI2 and SAVI (caused by a similar dropoff in NIR reflectance) that was not depicted in NDVI at the third time point. Site differences or the condition of plants within these plots might explain the decrease. Based on the lack of inconsistencies in the NDVI plots, we proceeded by considering the connection between NDVI and above ground biomass. Temporal changes of NDVI and above ground biomass at each of the six biomass sampling dates for each of the six intensive sampling plot areas are compared in Figure 1.18. Although the temporal lag (i.e., delay) between the increase in NDVI and the increase in biomass was not surprising, we did not model the temporal connection between NDVI and biomass in this study.

The NDVI trends of UAS, Sentinel, and Landsat sensors across the 2018 growing season are depicted in Figure 1.19. For each acquisition date (Table 1.2), we calculated summary statistics for NDVI within each

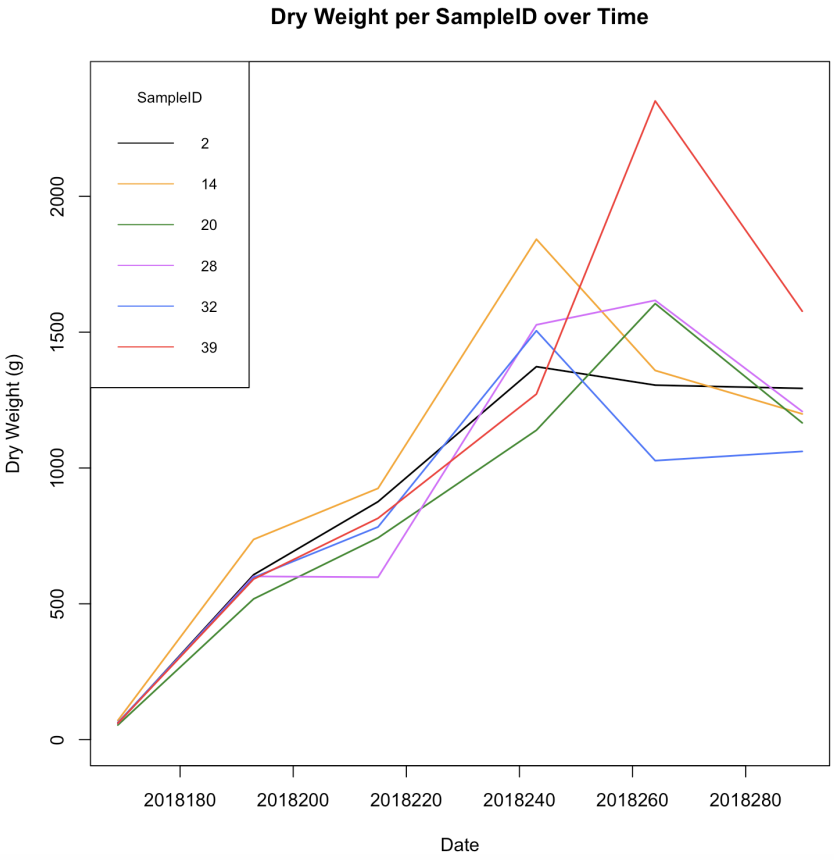

Figure 1.16: Above ground biomass dry weight measurements across the sampling dates for each sampling plot (SampleID)

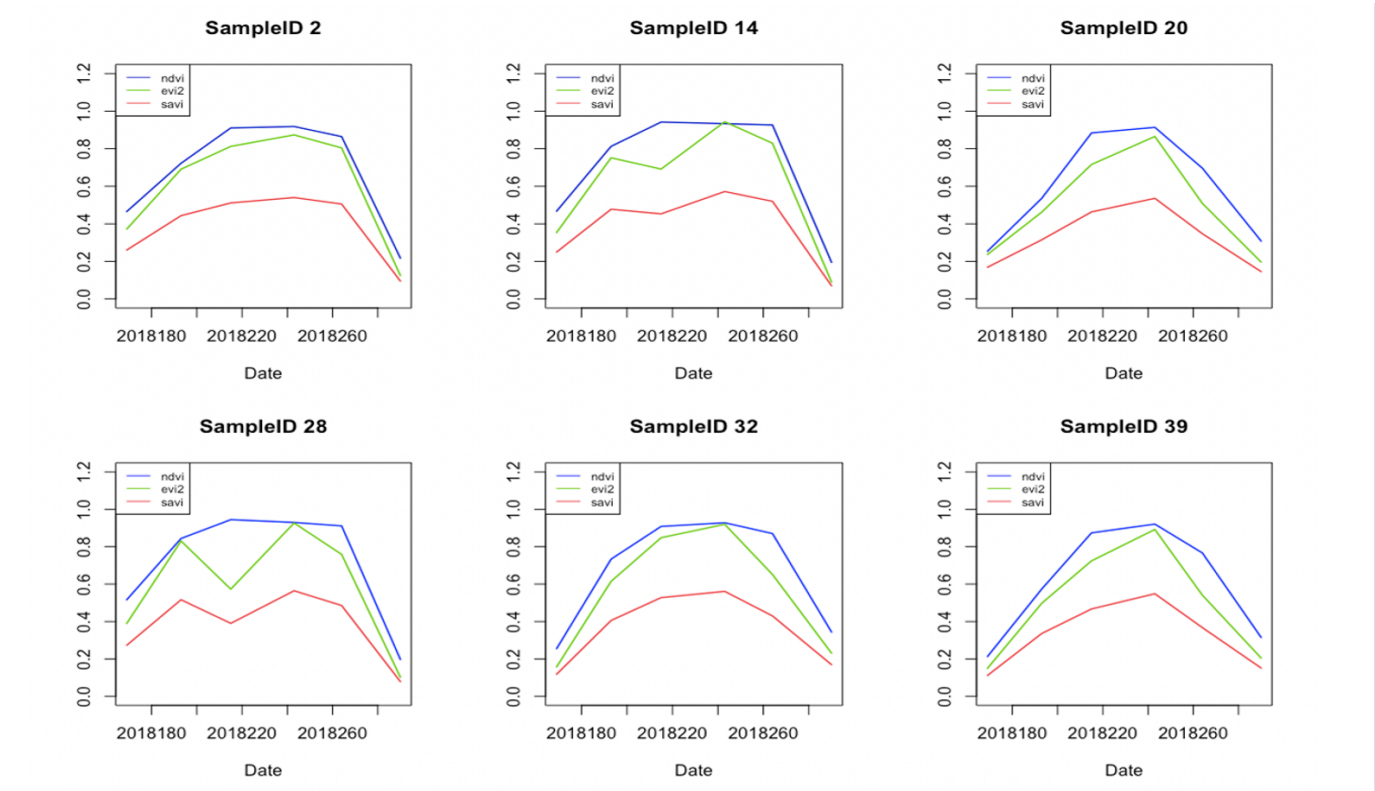

Figure 1.17: Temporal changes in NDVI, EVI2, and SAVI at each of the six intensive sampling plot areas

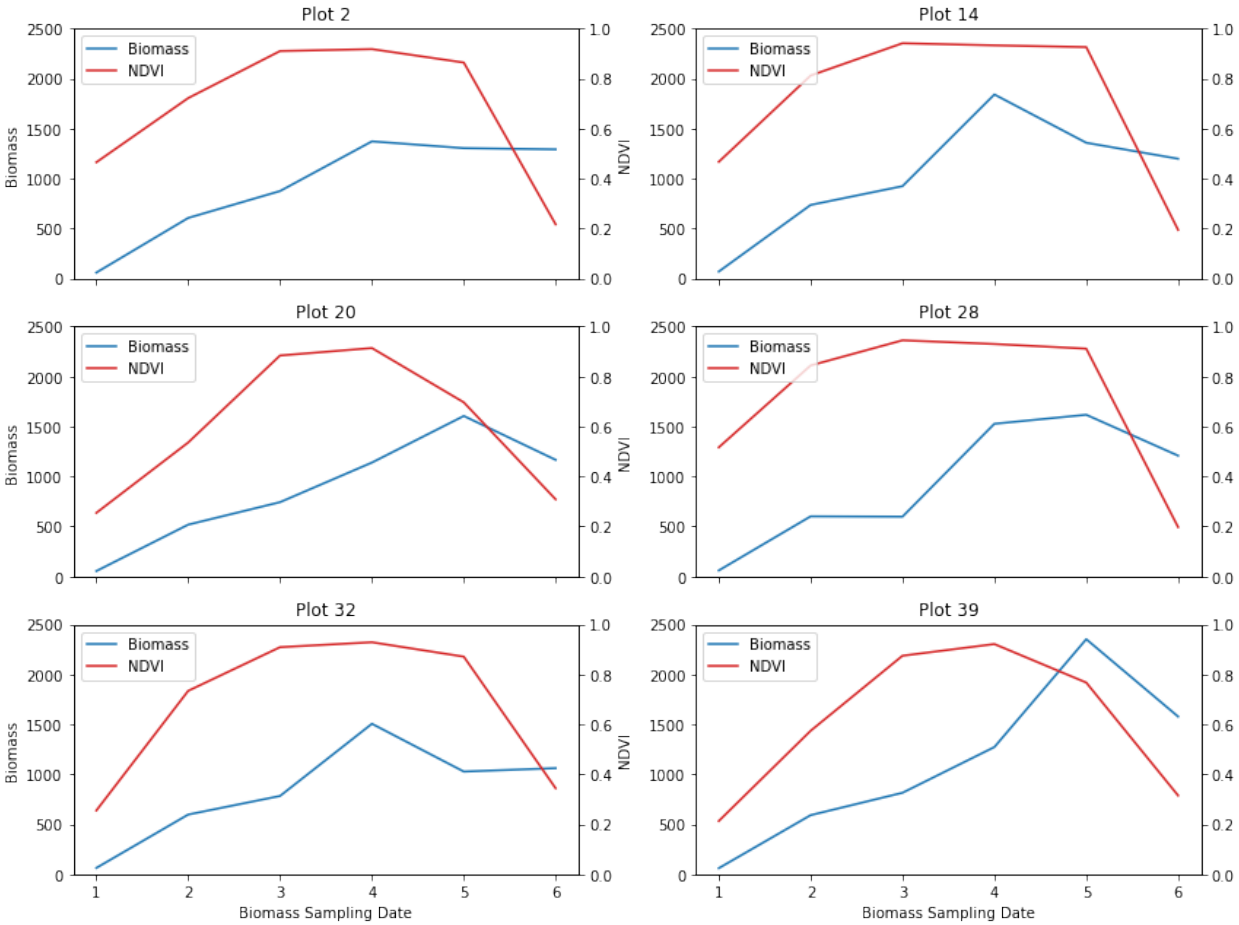

Figure 1.18: Temporal changes in NDVI and above ground biomass at each of the six intensive sampling plot areas

of the twenty-seven 30 m x 10 row plot areas within the cotton fields for each sensor. We then calculated each sensor's average and standard deviation of those twenty-seven measurements for each acquisition date. The trend lines in Figure 1.19 show the average NDVI value for each sensor on each acquisition date, while the error bars provide 95% confidence intervals. The Landsat readings for dates 4 and 5 were duplicates of dates 3 and 6, respectively, due to the lack of usable cloud-free imagery during August 2018. Also, the Sentinel reading for the third acquisition date was modified as given below to better illustrate the expected trendline of the NDVI values early in the growing season and to make up for a poor reading by the sensor due to cloudy weather conditions on the acquisition date. Because the Landsat measurements were more closely related to the Sentinel measurements during the early dates than the UAS measurements, we utilized the Landsat rate of change between dates 2 and 3 as a multiplier on the Sentinel measurement on the second acquisition date to recalculate the third Sentinel value. Regardless of the Sentinel measurement adjustment, this figure illustrates that satellite sensor NDVI readings substantially fall short of UAS sensor NDVI readings that are much closer to ground level. This can be attributed to differences in the sensors' bandwidths, atmospheric conditions (weather and clouds; scattering), and height of sensor, among others.

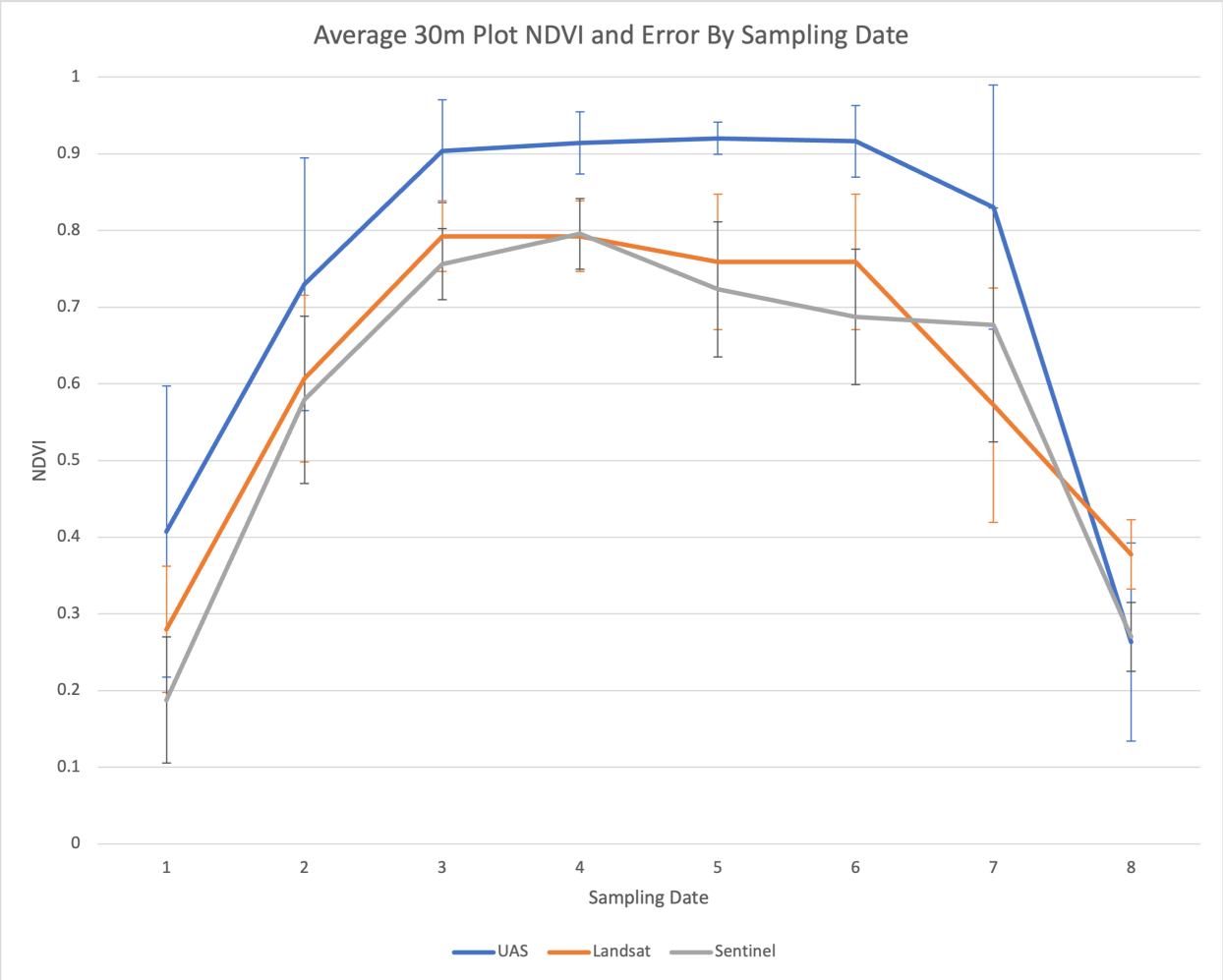

Figure 1.19: Comparison of NDVI values captured by UAS, Sentinel, and Landsat imagery. Error bars show 95% confidence intervals.

Chapter 2

Methodology

To tie together the satellite imagery and the UAS imagery, we borrowed some methods from climate studies. Global climate models describe coarse-scale patterns across large regions of the Earth. However, scientists are often interested in local climate patterns. Statistical downscaling produces finer-scale local climate measurements from coarse-scale global climate models (Jeong et al., 2012a,b; Washington, 2020). We used statistical downscaling to connect the coarse-scale satellite imagery with the finer-scale UAS imagery. In doing this, we attributed a portion of the Sentinel spectral reflectance information to each UAS pixel, in a process similar to downsampling. What we sought to create was a raster (a matrix of pixels organized into a grid with each cell containing coordinates and data value(s)) with the resolution of the UAS imagery, but with the downscaled spectral information from the satellite imagery.

The model created by Jeong et al. (2012a) is a two-part multivariate multisite statistical downscaling model (MMSDM): 1) a multivariate multiple linear regression (MMLR) model with 2) a spatially correlated stochastic downscaling component. We adapted the model proposed by Jeong et al. (2012a,b) to improve the notation and distributional assumptions. For n time records, m spatial sites, and k predictors,

the MMLR uses the model framework:

$$\mathbf{Y}_{n\times m} = \mathbf{X}_{n\times k} \cdot \mathbf{B}_{k\times m} + \mathbf{E}_{n\times m}, \tag{2.1}$$

where $\mathbf{Y}$ is the matrix of multivariate response variables, $\mathbf{X}$ is the standardized matrix of predictor variables, $\mathbf{E}$ is the error matrix, and $\mathbf{B}$ is the parameter matrix estimated via the standard Ordinary Least Squares (OLS) regression estimator:

$$\widehat{\mathbf{B}} = (\mathbf{X}^T\mathbf{X})^{-1}\mathbf{X}^T\mathbf{Y}. \tag{2.2}$$

The error matrix $\mathbf{E}$ follows the matrix normal distribution,

$$\mathbf{E} \sim \mathcal{MN}_{n\times m}(\mathbf{0}, \mathbf{U}, \mathbf{V}), \tag{2.3}$$

with zero mean matrix, and unknown covariance matrices $\mathbf{U}_{n\times n}$ and $\mathbf{V}_{m\times m}$. A random matrix which follows the matrix normal distribution is defined by a location (or mean) matrix and a set of two covariance matrices. The first of the two covariance matrices measures the covariance among the rows of the random matrix. Similarly, the second of the two covariance matrices measures the covariance among the columns of the random matrix. Based on the $n \times m$ construction of our random matrix $\mathbf{E}$, the rows represent time and the columns represent space. In this case, we can think of the two covariance matrices in the matrix normal distribution as representing temporal covariance ($\mathbf{U}$) and spatial covariance ($\mathbf{V}$), respectively.

The MMSDM uses the MMLR model to estimate the response variables, but the MMLR model can only predict the deterministic relationship between the response variables and the predictors. In other

words, the predicted response variables

$$\widehat{\mathbf{Y}} = \mathbf{X}\widehat{\mathbf{B}} \tag{2.4}$$

based on the OLS estimator retain no spatial relationship. This motivates the inclusion of the second part of the MMSDM: the spatially correlated stochastic downscaling component.

To correct for the lack of spatial correlation in the MMLR model, spatially correlated random noise augments the predicted response variables $\widehat{\mathbf{Y}}$. The observed error (residual) matrix is given by:

$$\widehat{\mathbf{E}} = \mathbf{Y} - \widehat{\mathbf{Y}}. \tag{2.5}$$

Then, $\widehat{\mathbf{E}}$ determines the temporally and spatially correlated stochastic downscaling component, which we defined as:

$$\mathbf{R} \sim \mathcal{MN}_{n\times m}(\mathbf{0}, \boldsymbol{\Theta}, \boldsymbol{\Sigma}), \tag{2.6}$$

where $\mathbf{R}$ follows the matrix normal distribution with zero mean matrix, temporal covariance matrix $\boldsymbol{\Theta}_{n\times n}$ equal to the covariance matrix of the rows of $\widehat{\mathbf{E}}$ (i.e., the covariance of the observed time records), and spatial covariance matrix $\boldsymbol{\Sigma}_{m\times m}$ equal to the covariance matrix of the columns of $\widehat{\mathbf{E}}$ (i.e., the covariance of the observed spatial sites). As we were interested only in the spatial correlation, we considered instead $\widetilde{\mathbf{R}}$, which we constructed by setting $\boldsymbol{\Theta} = \mathbf{I}$, where $\mathbf{I}$ is the identity matrix with elements of 1 along the diagonal and 0 otherwise. Finally, we added the stochastic component $\widetilde{\mathbf{R}}$ to our deterministic MMLR model to give $\widetilde{\mathbf{Y}}$, the spatially correlated response variables:

$$\widetilde{\mathbf{Y}} = \widehat{\mathbf{Y}} + \widetilde{\mathbf{R}}. \tag{2.7}$$

Jeong et al. (2012a) used the MMSDM to downscale minimum and maximum temperature in southern Quebec, while Jeong et al. (2012b) expanded the analysis by downscaling precipitation probability and precipitation amount in the same region. In both papers, the downscaled variables were correlated. This two-part model design ensureed that the spatial correlation structure of the downscaled variables remained after the procedure. Washington (2020) applied this methodology to downscale temperature, precipitation, and solar radiation at multiple sites in Puerto Rico, while also expanding the work by recommending a post hoc locally estimated scatterplot smoothing (LOESS) quantile mapping (LQM) bias correction term:

$$\widetilde{\mathbf{Y}}_{Corrected} = \widetilde{\mathbf{Y}}_{Raw} + l(\widetilde{\mathbf{Y}}_{Bias}), \tag{2.8}$$

where $l(\cdot)$ represents the LOESS estimate of bias magnitude. Global climate models are known to project too many low-magnitude precipitation events to occur compared to historical observations, for example. This systematic bias can be corrected using the above downscaling methodology. A bias correction can also be useful in remote sensing, where bias may exist spatially, temporally, or based on scale (Kornelsen et al., 2015; Njuki et al., 2020; Pan et al., 2018).

This MMSDM approach uses linear regression to downscale climate variables, then introduce samples from a parametric error distribution in order to fine-tune the spatial correlation. Therefore, these final spatially correlated response variable predictions are dependent not only on the parametric error distribution assumptions imposed, but also on the randomly sampled cross-correlation error matrix.

Statistical downscaling of global climate models typically makes predictions at a discrete number of ground surface points. While this framework is a reliable method for ensuring spatial correlation remains after downscaling, the implementation is computationally infeasible when treating each UAS image pixel

as a spatial site. In addition, we would like to be able to analyze our data as is, without the need for random samples from a parametric error distribution. Therefore, we propose two alternative methods to construct a grid of predictions by treating each UAS pixel as a spatial site: (1) regression kriging and (2) artificial augmentation. We further propose two novel sets of statistical downscaling predictions by combining the regression kriging and artificial augmentation procedures.

2.1 Regression Kriging

Our first statistical downscaling method comes from regression kriging (Hengl et al., 2004, 2007; Meng et al., 2013; Odeh et al., 1995). RK is a spatial prediction technique that combines regression and interpolation when the response variable is spatially correlated with environmental factors. The response variable is modeled as a function of the explanatory variable(s) in a standard OLS framework (we use OLS here as an illustrative example, though a more complex regression model can be implemented), then a spatial variogram model is fit on the residuals to determine the kriging weights and to interpolate between spatial sites. The generic formulation for the prediction of the target variable $z(s)$ at location s is:

$$z(s) = m(s) + e(s), \tag{2.9}$$

where $m(s)$ is the regression component and $e(s)$ is the residual component. With the regression and residual components separated, we can first consider the regression component:

$$m(s) = \sum_{k=0}^{p} \beta_k \cdot q_k(s) + \epsilon, \tag{2.10}$$

where β_k are the regression model parameters, $q_k(s)$ are the values of the p explanatory variables at the target location (with $q_0(s) = 1$ as an intercept term), and $\epsilon \sim N(0, \omega)$ is the regression error assumed to be normally distributed with mean 0 and unknown variance ω. The regression model parameters are estimated via:

$$\widehat{\beta} = (Q^T Q)^{-1} Q^T \mathbf{z}, \tag{2.11}$$

where $\widehat{\beta} = [\widehat{\beta}_0 \ \ \widehat{\beta}_1 \dots \widehat{\beta}_p]^T$ are the regression model parameter estimates; $Q = [\mathbf{1} \ \ \mathbf{q_1} \dots \mathbf{q_p}]$ is the predictor matrix; $\mathbf{1}$ is a vector that has all elements of 1; $\mathbf{q_k} = [q_k(s_1), q_k(s_2), \dots, q_k(s_n)]^T$, $k = 1, \dots, p$, is the vector of explanatory variable values from the observed sites $s_1, s_2, \dots, s_n$; and $\mathbf{z} = [z(s_1), z(s_2), \dots, z(s_n)]^T$ is the vector of observed response variable values from the observed sites. RK produces response predictions in the form:

$$\hat{z}^{RK}(s) = \widehat{m}(s) + \hat{e}(s) = \sum_{k=0}^{p} \widehat{\beta}_k \cdot q_k(s) + \sum_{i=1}^{n} \lambda_i \cdot e(s_i), \tag{2.12}$$

where $\hat{z}^{RK}(s)$ is the predicted value of the response variable at an unvisited location s; $\widehat{m}(s)$ is the fitted regression component; $\hat{e}(s)$ is the interpolated residual component; $\widehat{\beta}_k$ are the estimated regression model coefficients; $q_k(s)$ are the values of explanatory variables at the target location (with $q_0(s) = 1$); λ_i are the kriging weights determined by the spatial correlation structure of the residuals (details to follow); and $e(s_i) = z(s_i) - \widehat{m}(s_i)$ are the residuals of the sample data $z(s_1), \dots, z(s_i), \dots, z(s_n)$ at sample sites $s_1, \dots, s_i, \dots, s_n$. The $\widehat{m}(s)$ component is analogous to $\widehat{\mathbf{Y}}$ in Equation 2.7; similarly, the $\hat{e}(s)$ is analogous to $\widetilde{\mathbf{R}}$ in Equation 2.7, except here we calculated the weighted average of the residuals with the kriging weights as our additive term to modify the OLS predicted values. In this case, our spatially correlated response variable predictions still relied on the spatial covariance structure of the residuals, but

they utilized the weighted average of the residuals with the kriging weights instead of a random sample from the parametric error distribution.

Spatial autocorrelation is driven by the variogram (Matheron, 1963; Cressie, 1993; Wikipedia, 2024), which is given as a function of the lag – the distance between two measurement sites. Three other important characteristics of a variogram are the sill, nugget, and range (Figure 2.1). The sill is the limit of the variance between two observations as the distance between the sites grows larger. The nugget is the variance of the difference in observations taken at the same site (lag 0). Theoretically, the nugget value should be zero. When it is not zero, it is interpreted as microscale variation, measurement error, or both. Finally, the range is the length of spatial dependence; observations more than this distance apart are assumed to be uncorrelated.

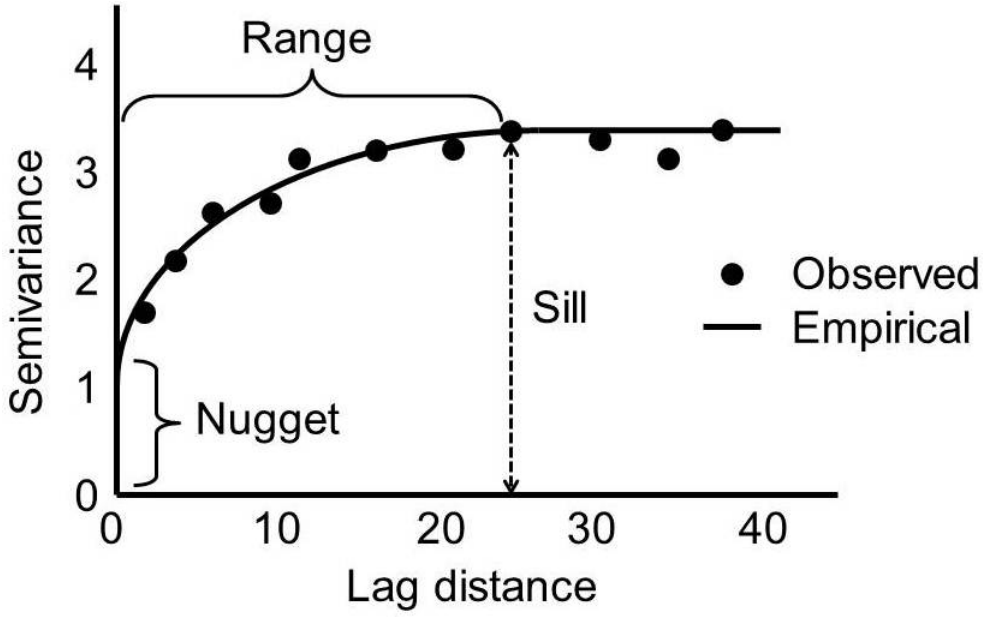

Figure 2.1: The sill, nugget, and range define the behavior of the variogram. [Source: Biswas and Si (2013)]

Our variograms were fit using residuals from the OLS model. Once the residuals were obtained, they were grouped into a specified number of bins sorted by lag distance. The sample variogram was then

constructed based on the sample variance observed within each bin. Assuming the trend in the data had been removed from the residuals by the OLS model (Equation 2.10), the sample variogram should level off at the sill. Next, we fit variogram models to the sample variogram. We chose Spherical and Matérn models for their flexibility to model most sample variograms (Isaaks and Srivastava, 1989; Goovaerts, 1997). The Spherical variogram model is given by:

$$v(h) = \begin{cases} \sigma_0 + \sigma^2\left(\frac{3}{2}\frac{h}{r} - \frac{1}{2}\left(\frac{h}{r}\right)^3\right) & h \leq r \\ \sigma_0 + \sigma^2 & h > r \end{cases}, \tag{2.13}$$

where h is the lag, σ_0 is the nugget, $\sigma^2 + \sigma_0$ is the sill, and r is the range. The Matérn variogram is given by:

$$v(h) = \sigma^2\left(1 - \frac{1}{2^{\nu-1}\Gamma(\nu)}\left(\frac{h}{r}\right)^{\nu} K_\nu\left(\frac{h}{r}\right)\right) + \sigma_0, \tag{2.14}$$

where h is the lag, σ_0 is the nugget, $\sigma^2 + \sigma_0$ is the sill, r is the range, ν is the smoothness parameter, Γ is the gamma function, and K_ν is the modified Bessel function of the second kind of order ν (Abramowitz and Stegun, 1964):

$$K_\nu(x) = \frac{\pi}{2\sin\nu\pi}\left\{\sum_{m=0}^{\infty}\frac{1}{m!\Gamma(m-\nu+1)}\left(\frac{x}{2}\right)^{2m-\nu} - \sum_{m=0}^{\infty}\frac{1}{m!\Gamma(m+\nu+1)}\left(\frac{x}{2}\right)^{2m+\nu}\right\}. \tag{2.15}$$

We visually determined which variogram model fit the sample variogram better. Finally, we reran the RK fitting procedure, this time with the fitted spatial variogram model included to adjust the kriging weights of the observed residuals. The kriging weights become:

$$\lambda = \mathbf{C}^{-1} \cdot \mathbf{c}, \tag{2.16}$$

where $\lambda = [\lambda_1 \quad \dots \quad \lambda_n]^T$ is the vector of kriging weights used in Equation 2.12 with the kriging weights summing to 1; $\mathbf{C}$ is the covariance matrix of all pairs of sample sites $s_1, \dots, s_n$; and $\mathbf{c}$ is the vector of covariances between the predicted response at s and the sample sites (Hengl, 2009).

The samples we used to fit the model were highly spatially concentrated, confined to the six sampling plot areas (plots 2, 14, 20, 28, 32, and 39 in Figure 1.14). Because of this, we could not smoothly interpolate the spatial information between sites. Instead, we observed a starburst visual effect of spatial information spreading away from the sampled areas (Figure 2.2). While this effect appears to be a problem with the kriging procedure, kriging is statistically robust (Wang et al., 2019; Tuo and Wang, 2020). The problem lies in the limited sampling at only six concentrated sites across the fields. We used the RK model to generate predictions at sites much more spread out than the spatially dense data used to fit the model. The best prediction the RK model can provide any particular location is based on the edge of the sampling plot closest to that location, which is why similar prediction values seem to radiate out of the sampling plot areas.

2.2 Artificial Augmentation

Our second statistical downscaling method is built upon an ad-hoc artificial augmentation (AA) algorithm, a version of data fusion to synthetically increase the resolution of satellite imagery. Since each satellite pixel can contain thousands of UAS pixels, using the single satellite value as a downscaling predictor will not produce a variety of response values at the UAS level. Therefore, we used the UAS pixel data to introduce spatial variation in the satellite pixel data, which could then be downscaled to the UAS level as a change of support via a standard OLS model. First, each satellite pixel was downsampled into pixels matching

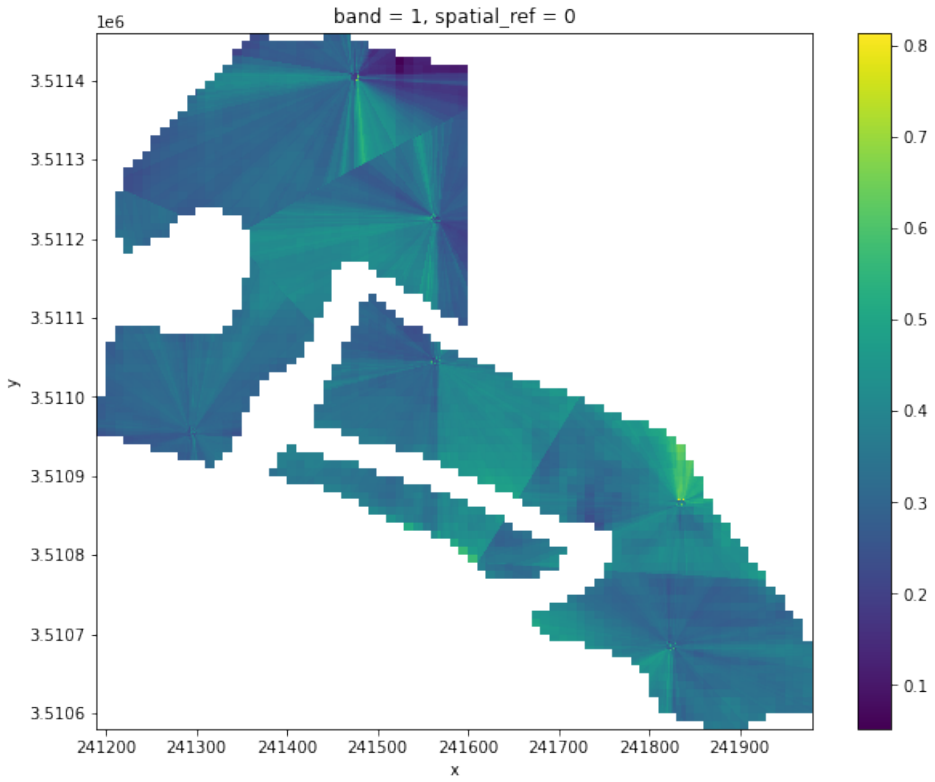

Figure 2.2: The regression kriging predictor possesses a starburst visual effect as the predictions were extrapolated from the sampling plots

the resolution of the UAS pixels, where each of the smaller pixels was assigned the value of the larger pixel. Next, we calculated the average value of the UAS pixels within the boundary of the satellite pixel. Then, we used the ratio of each individual UAS pixel to that average as a weight coefficient on the satellite value to assign a reweighted value to the downsampled satellite pixels. Finally, we downscaled the reweighted satellite data through OLS to match the distribution of values in the UAS pixels. The AA model takes the form:

$$z(s) = \beta_0 + \beta_1 \cdot w(s) + \epsilon, \tag{2.17}$$

where $z(s)$ is the value of the response variable at pixel s, β_0 and β_1 are the regression model parameters, $\epsilon \sim N(0, \omega)$ is the regression error assumed to be normally distributed with mean 0 and unknown variance ω, and $w(s)$ is the reweighted satellite value at pixel s, given by:

$$w(s) = \frac{u(s) \cdot q(S)}{\sum_{i=1}^{n} u(s_i)/n}, \tag{2.18}$$

where $u(s_i)$ are the UAS values at pixels $s_1, \ldots, s, \ldots, s_n$ within satellite pixel S and $q(S)$ is the original satellite value at pixel S. We fit the downscaled regression model parameters by:

$$\widehat{\beta} = (W^T W)^{-1} W^T \mathbf{z}, \tag{2.19}$$

where $\widehat{\beta} = [\widehat{\beta}_0 \ \ \widehat{\beta}_1]^T$ are the regression model parameter estimates; $W = [\mathbf{1} \ \ \mathbf{w}]$ is the predictor matrix; $\mathbf{1}$ is a vector that has all elements of 1; $\mathbf{w} = [w(s_1), w(s_2), \ldots, w(s_n)]^T$ is the vector of all reweighted Sentinel pixel values from the observed sites $s_1, s_2, \ldots, s_n$; and $\mathbf{z} = [z(s_1), z(s_2), \ldots, z(s_n)]^T$ is the vector of observed values of the response variable from the observed sites. Reweighted and downscaled response predictions take the form:

$$\hat{z}^{AA}(s) = \widehat{\beta}_0 + \widehat{\beta}_1 \cdot w(s). \tag{2.20}$$

We created a third statistical downscaling predictor by applying the reweighting portion of the AA algorithm to the RK results, replacing $q(S)$ in Equation 2.18 with $\bar{z}^{RK}(S) = \frac{1}{n} \sum_{i=1}^{n} \hat{z}^{RK}(s_i)$, the average of all pixel values $\hat{z}^{RK}(s_i)$ from Equation 2.12 for pixels $s_i \in S$ within the boundary of Sentinel pixel S. This process reintroduced the extrapolated RK downscaled values to the spatial variation found

in the UAS values, which produced regression kriging artificial augmentation (RKAA) predicted values in the form:

$$\hat{z}^{RKAA}(s) = \frac{u(s) \cdot \bar{z}^{RK}(S)}{\sum_{i=1}^{n} u(s_i)/n}. \tag{2.21}$$

We took our statistical downscaling predictors one step further by creating a fourth predictor: an average of the three (RK, AA, and RKAA), given by

$$\hat{z}^{Joint}(s) = \frac{\hat{z}^{RK}(s) + \hat{z}^{AA}(s) + \hat{z}^{RKAA}(s)}{3}. \tag{2.22}$$

We believe all of our statistical downscaling predictors are biased; therefore, we believe that taking the average of the three will balance out that bias by reining in the worst of the biases, leaving us with a joint predictor that takes advantage of the best parts of the individual predictors while smoothing out the worst parts.

Our above ground biomass measurements were limited to six measurements via the six sampling plots. Thus, we again utilized our AA algorithm reweighting procedure (Equation 2.18) to distribute the biomass value at each 30 m x 10 crop row sampling plot to a large multitude of UAS resolution pixels within the boundary of the biomass plot weighted by UAS pixel values:

$$b(s) = \frac{u(s) \cdot b(P)}{\sum_{i=1}^{n} u(s_i)/n}, \tag{2.23}$$

where $b(s)$ is the weighted biomass at site s, $b(P)$ is the biomass per pixel measurement for sampling plot P, and $u(s_i)$ are UAS pixel measurements at sites $s_i \in P$ within the sampling plot area. The workflow to produce weighted biomass values for each UAS pixel from the biomass per plot as an initial input is

outlined in Figure 2.3. We then fit four OLS models, with each statistical downscaling method used as a single predictor, to create predictions of cotton above ground biomass:

$$\hat{b}^{RK}(s) = \widehat{\beta}_0 + \widehat{\beta}_1 \cdot \hat{z}^{RK}(s), \tag{2.24}$$

$$\hat{b}^{AA}(s) = \widehat{\beta}_0 + \widehat{\beta}_1 \cdot \hat{z}^{AA}(s), \tag{2.25}$$

$$\hat{b}^{RKAA}(s) = \widehat{\beta}_0 + \widehat{\beta}_1 \cdot \hat{z}^{RKAA}(s), \tag{2.26}$$

$$\hat{b}^{Joint}(s) = \widehat{\beta}_0 + \widehat{\beta}_1 \cdot \hat{z}^{Joint}(s). \tag{2.27}$$

2.3 Simulation

2.3.1 Spatial Random Fields and Variograms

To test the validity of our statistical downscaling methods as predictors, we created a simulation to mimic the real-world scenario. We set up the simulation by first taking a grid space of $[0, 10]$ on the x-axis and $[-5, 5]$ on the y-axis, with 0.05 horizontal spacing and 0.05 vertical spacing between grid points, for a total of $40,401$ measurement sites. We then introduced spatial autocorrelation via a spatial random field (SRF). We created a spatial random field to represent each of X_1, X_2, and ϵ, our two predictors and the error term, respectively. X_1 and X_2 were independent explanatory variables (e.g., soil composition and leaf area index) used to predict the response variable (e.g., above ground biomass). Each point in the grid space was then assigned values based on those SRFs. We utilized the Exponential model as the underlying

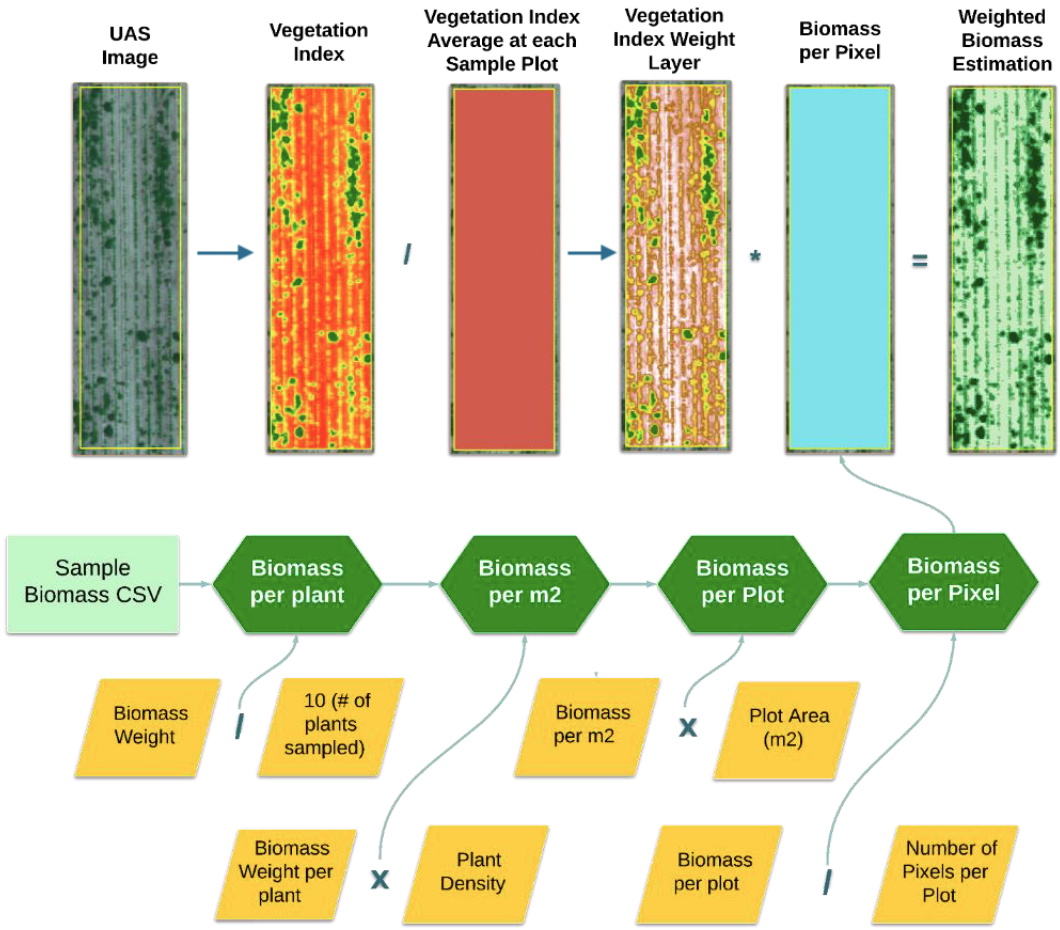

Figure 2.3: Workflow implemented to create a weighted biomass raster from the single biomass sample and the UAS measured NDVI over the 30 m x 10 row biomass sampling plot. Biomass data are publicly available in Ag Data Commons (Coffin et al., 2023). [Source: Stone (2023)]

distribution in the SRF. The Exponential model is given by the variogram:

$$v(h) = \sigma^2\left(1 - exp\left(-s * \frac{h}{r}\right)\right) + \sigma_0, \tag{2.28}$$

where h is the lag, σ_0 is the nugget, $\sigma^2 + \sigma_0$ is the sill, r is the range, and the standard rescale factor is $s = 1$.

Having assigned values for X_1, X_2, and ϵ to each point in our grid space, we moved on to calculating our simulated response variable Y at each site:

$$Y = \beta_0 + \beta_1 X_1 + \beta_2 X_2 + \epsilon. \tag{2.29}$$

We assigned $\beta = [\beta_0, \beta_1, \beta_2]$ as the intercept term and coefficients on X_1 and X_2, respectively. We used $\beta = [0.1, 0.25, 0.25]$ to create the grid of Y values to represent the ground level biomass. To create an intermediate level of Y values between the satellite and ground levels, we simulated a UAS-level grid of Y values via a misspecified version of the model in Equation 2.29:

$$Y^* = \beta_0 + \beta_1 X_1 + \epsilon. \tag{2.30}$$

This set of values maintained a similar spatial structure to the ground level response, but was not a direct copy of those values. In practice, this constructed data represents a situation where UAS imagery can detect some variables (e.g., leaf area index), but not others (e.g., soil composition).

Aggregating the SRF information from a grid of points to a grid of pixels involveed careful manipulation of shapefiles and rasters. We began by using the GeoPandas Python package to convert a grid of points into a GeoDataFrame. GeoDataFrames behave much like DataFrames in Pandas, but include geospatial information that links data together spatially. Our GeoDataFrame not only contained all prior information on position based on the x- and y-axis, as well as the field value at those positions, but also increased functionality concerning how these points interacted spatially. Next, we used shapefiles to define

the grid of pixels we eventually wanted to produce as part of our raster. We defined the maximum and minimum x and y coordinate points in our grid space, and divided the range evenly to produce a grid of polygons that covered our grid space. Then, we utilized the spatial join property of our GeoDataFrame to allow the polygons to determine which grid space positions fell within their boundary. The polygon values populated by taking the average of all points that fell within their boundary. Finally, we converted the grid of polygons to a raster for plotting and analysis.

We assigned each 2x2 section of the grid space to be a satellite pixel. For the UAS level pixels and ground level pixels, we chose a pixel size of 0.05 by 0.05. This resulted in 25 satellite pixels, $40,000$ UAS pixels, and $40,000$ ground pixels. Examples of the satellite level pixels and the finer-scale pixels are shown in Figure 2.4. The ground level pixels were used to represent the true behavior of the ground level response variable. The UAS level pixels depicted behavior similar, but not identical, to the ground level data; in addition, the satellite pixel boundaries showed how the UAS pixels were divided into groupings of 1600 pixels per satellite pixel. Finally, the satellite pixels illustrated the loss of spatial information from coarser resolution.

2.3.2 Simulated Statistical Downscaling and Biomass Prediction

To replicate the real-world scenario we faced with limited sampling, we created a sampling scheme that utilized concentrated samples with the ability to extrapolate to other areas of the study area. We compiled 1600 UAS level pixels per satellite pixel square of data shaded in Figure 2.5, resulting in 6400 total pixels samples used to fit our models as the response variable. This sampling strategy mimics the real-world scenario we will study in Chapter 3 by sampling evenly across the study site. Due to the computational expense of RK, this sampling scheme included a representative sample of data without overwhelming the

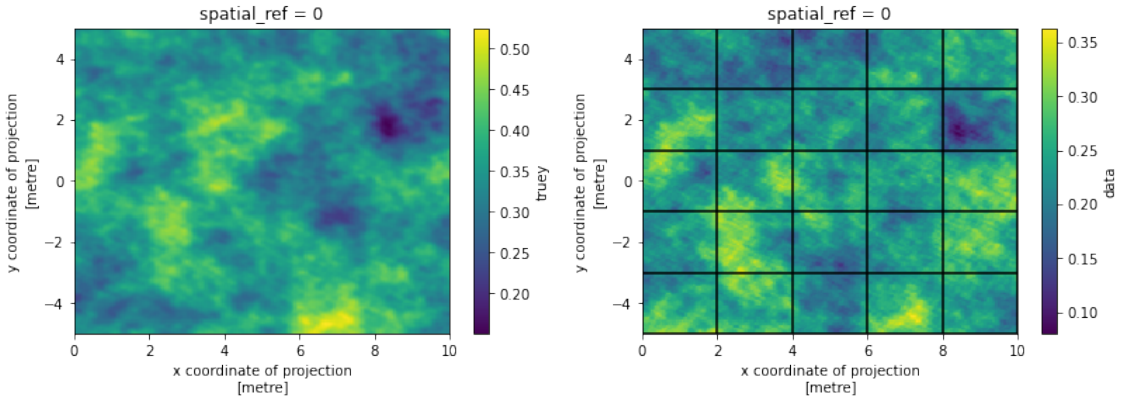

(a) Simulated ground level pixels

(b) Simulated UAS level pixels with satellite pixel boundaries overlaid

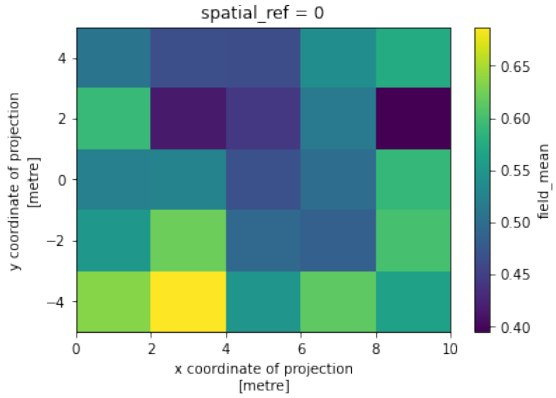

(c) Simulated satellite level pixels

Figure 2.4: Illustration of the different simulated resolutions

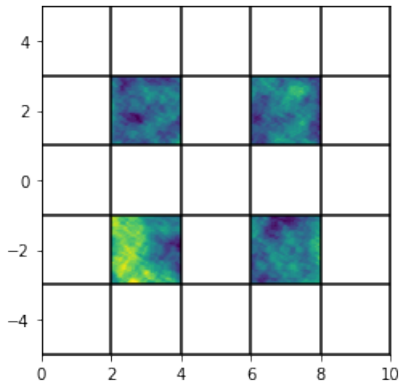

Figure 2.5: Simulation sampling scheme: all response variable data and explanatory variable data was collected from the shaded areas.

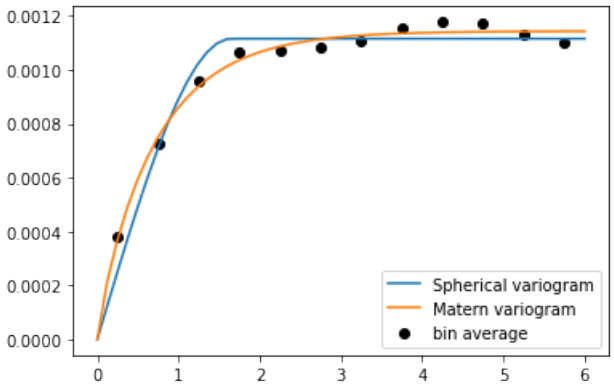

Figure 2.6: Simulation sample variogram with fitted Spherical and Matérn variogram curves

RK model. We started the RK modeling process by first fitting an OLS regression between the response variable data compiled above and the satellite level predictor data from the same four sampled areas in Figure 2.5. We then calculated the OLS residuals and fit the variogram models in Equations 2.13 and 2.14. The sample variogram with fitted variogram curves is depicted in Figure 2.6.

We moved on to running our downscaling procedures to produce four predictors for the simulated ground level biomass. Using the model parameters that were fit using the samples described above, we created predictions at the unsampled locations not shaded in Figure 2.5. The four downscaled predictors

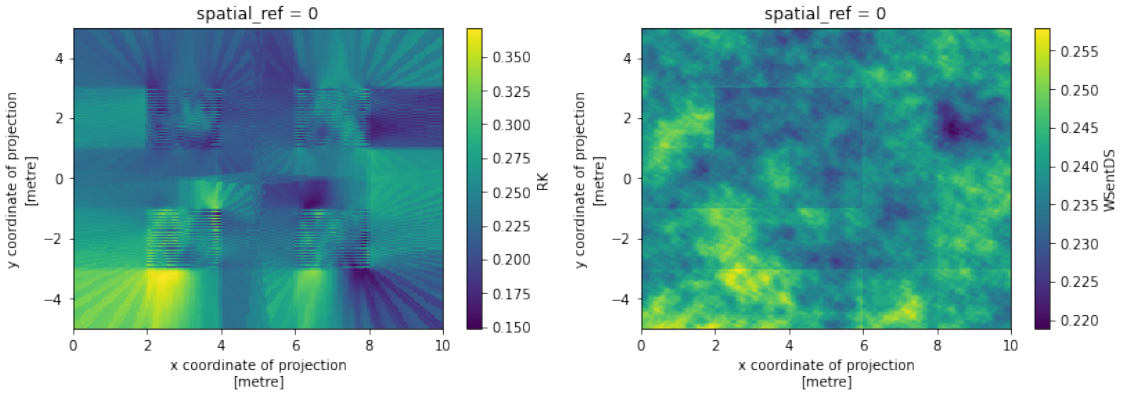

(a) Regression kriging

(b) Satellite artificial augmentation

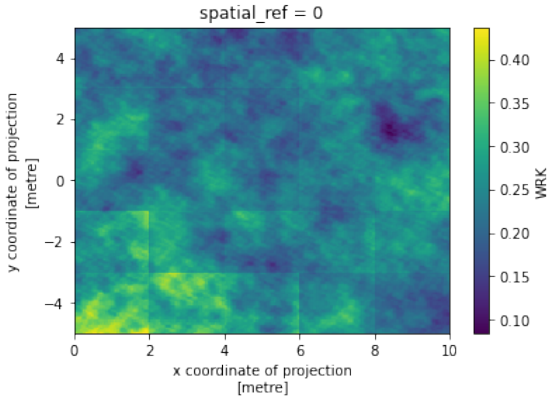

(c) Regression kriging artificial augmentation

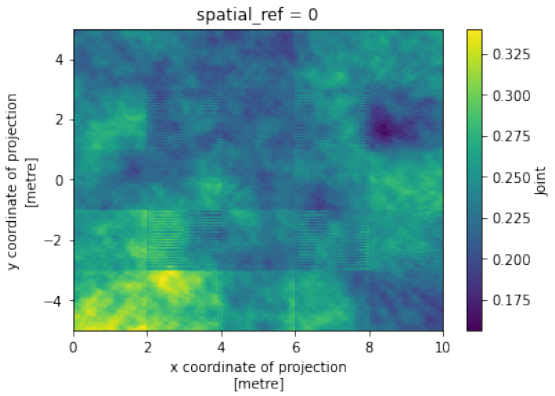

(d) Joint predictor

Figure 2.7: Four simulated downscaled predictors from satellite level data

are shown in Figure 2.7. Notice in the RK frame of Figure 2.7 (panel a) that the starburst effect was still present in our simulation due to the concentrated samples used to fit the model. The other predictors did not experience the starburst effect because they did not spatially extrapolate predictions from the sampled locations with kriging.

We used these four predictors in separate OLS models and gauged their ability to predict the simulated ground level biomass. The predictions of simulated ground level biomass (in g/pixel) produced by each predictor are shown in Figure 2.8. Because of the simple nature of the OLS models, the four biomass

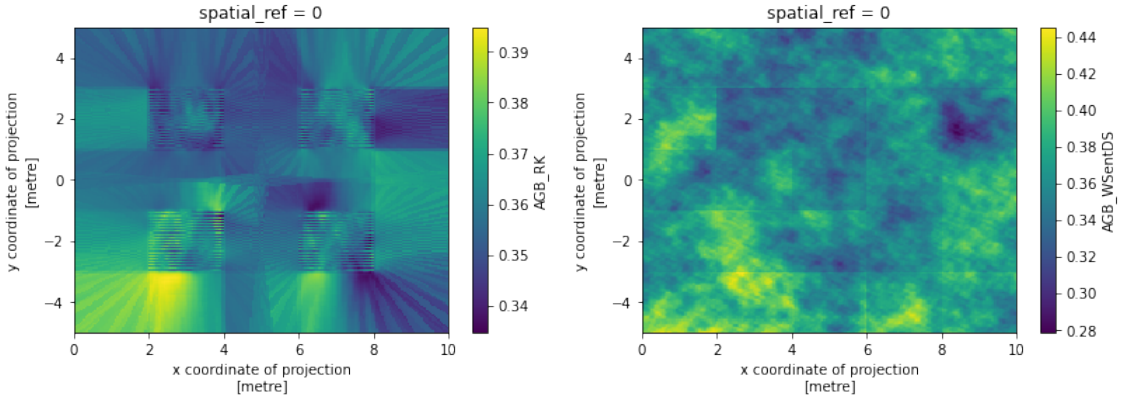

(a) Regression kriging

(b) Satellite artificial augmentation

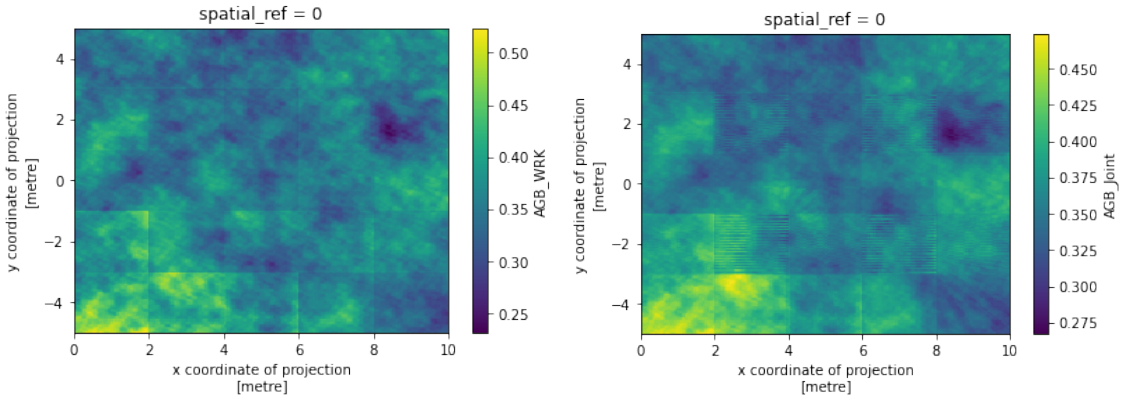

(c) Regression kriging artificial augmentation

(d) Joint predictor

Figure 2.8: Simulated ground level biomass predictions (in g/pixel) from the four predictors

predictions appear similar to their predictors, with an additive shift factor and a multiplicative scale factor connecting the two. The biomass prediction values from each method fell within a similar neighborhood, with the satellite AA prediction having the least spread and the RKAA prediction having the most.

To measure the performance of the four downscaled predictors, we compared the predictors against the closest "ideal" predictor we had: the simulated UAS level data from the misspecified model in Equation 2.30. The predicted ground level biomass from using the UAS level data as the OLS predictor with the same sampling scheme as the other four predictors is shown in Figure 2.9. The mean squared error (MSE)

descriptive statistics for the five predictors, detailed in Table 2.1, were calculated from 100 simulations[1]. Additionally, the violinplot for each predictor with the associated boxplot inlaid is depicted in Figure 2.10. Violinplots offer an upgrade from standard boxplots by showcasing the kernel density distribution of the observations in addition to the standard boxplot quartiles. As expected, the RK performed worst, due mainly to the limited and concentrated sampling points. The satellite AA predictor typically generated the lowest MSE of the four statistical downscaled predictors, perhaps because this method benefited from the effect of downscaling after the AA reweighting process had been applied. The RKAA, as an enhancement of the original RK predictor, typically produced MSE values between RK and satellite AA. The joint predictor, defined as a simple average of the other three predictors, typically realized MSE values around the average of the MSE values of the other three predictors. The joint predictor fell short of the two AA predictors due to the inclusion of the standard RK predictor; as the RK predictor improves, so too shall the joint predictor. Finally, we saw that all four RK and AA predictors fell short of the measurements produced by the UAS level "ideal" predictor. These simulations honed our expectations for the behavior of the predictors when applied to real satellite, UAS, and ground level data.

[1]During the creation of the 100 simulations, an additional simulation was run to replace one of the first 100 simulations that experienced fitting problems. More details can be found in Appendix A.

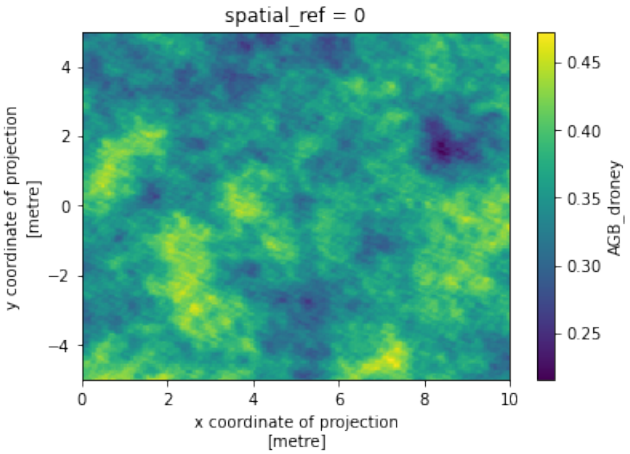

Figure 2.9: Predicted biomass from simulated UAS level data

Table 2.1: Mean squared error statistics from 100 simulations

	Regression kriging	**Satellite artificial augmentation**	**Regression kriging artificial augmentation**	**Joint predictor**	**UAS level "ideal" predictor**
count	100	100	100	100	100
mean	0.003198	0.002017	0.002416	0.002697	0.001457
std	0.000787	0.000515	0.000761	0.000797	0.000276
min	0.001914	0.001106	0.000982	0.001157	0.000852
25%	0.002665	0.001709	0.001813	0.002112	0.001246
50%	0.003005	0.001950	0.002325	0.002599	0.001418
75%	0.003541	0.002313	0.002895	0.003189	0.001641
max	0.006715	0.003896	0.004280	0.004834	0.002119

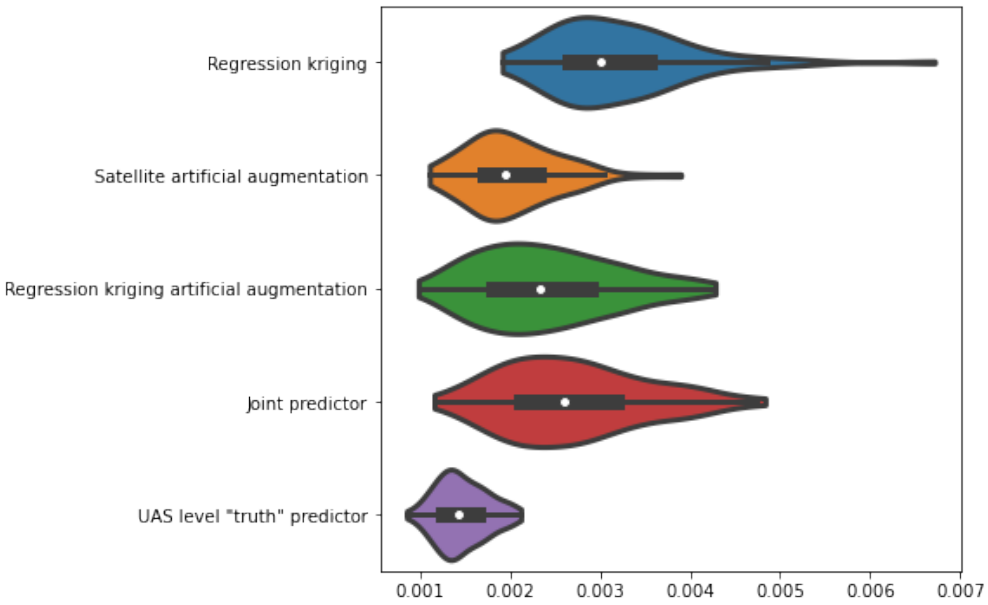

Figure 2.10: Mean squared error violinplots from 100 simulations, with boxplots inside the violin areas.

Chapter 3

Analysis

We began our analysis of the ACF satellite, UAS, and ground level data by first noting that the crop rows in the upper field were aligned in a different direction than the crop rows in the lower pair of fields. The differing directions could have some impact on crop growth. Because of this, we decided to analyze the upper field separately from the lower two fields. Also, due to time and computation constraints, all of the following analysis made use of only the first sampling/acqusition date of the 2018 growing season (above ground biomass and UAS imagery from June 18 and Sentinel imagery from June 11). Additionally, we focused our attention on modeling the relationship between NDVI and above ground biomass (Figure 1.18) based on the exploratory data analysis in Section 1.2.

3.1 Regression Kriging

Analyzing the whole farm altogether when treating each pixel as a spatial location was computationally infeasible due to the sheer number of UAS pixels. We parsed through the field systematically using the

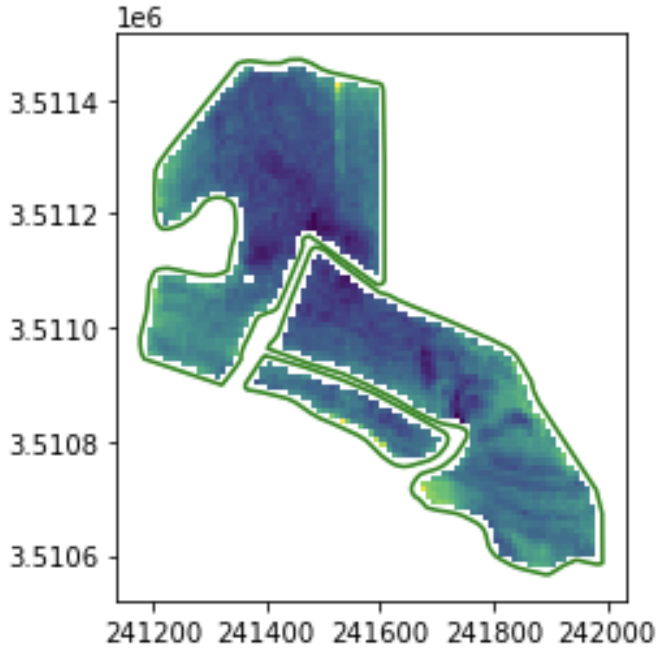

Figure 3.1: ACF Sentinel pixel polygons after edge pixel and 'no data' pixel removal, with the original field boundary shown in green.

Sentinel pixel polygons as a grid. The Sentinel pixel polygons of the ACF that remained after processing out the edge pixels and 'no data' pixels are shown in Figure 3.1. We removed Sentinel pixels where the associated size provided fewer than 100x100 UAS pixels per Sentinel pixel (mainly removing edge pixels that had been rendered incomplete by raster clipping processes) and those that had been assigned values of 'no data' (one particular section of the upper field contained a ground control point that was processed as 'no data', which caused the two-pixel hole in the upper field). This removal system left us with $1,281$ Sentinel pixels in the upper field and $1,278$ Sentinel pixels in the lower fields, which equated to about 25.6 million UAS pixels total.

From here, we used downsampled Sentinel pixels formed by subdividing the Sentinel pixel into smaller pixels matching the UAS pixel size and assigned the Sentinel pixel NDVI value to each of the smaller pixels

within the Sentinel boundary in order to establish a one-to-one correspondence between the Sentinel and UAS pixels. Due to the computational intensity of RK, we chose to limit the scope of our observed data to the 100x100 UAS pixel area that coincided with the Sentinel pixel at the center of each of the six biomass sampling plot areas. Using the combination of UAS pixels within these areas and the Sentinel pixel values downsampled at those UAS pixels, we proceeded with our statistical downscaling methodology by first creating a linear regression of downscaled Sentinel pixel NDVI values as a function of the original Sentinel pixel NDVI values:

$$m(s) = \beta_0 + \beta_1 \cdot q(s) + \epsilon, \tag{3.1}$$

where $m(s)$ is the OLS downscaled Sentinel NDVI value at pixel s, $q(s)$ is the original Sentinel pixel NDVI value, β_0 and β_1 are the regression parameters, and $\epsilon \sim N(0, \omega)$ is the regression error assumed to be normally distributed with mean 0 and unknown variance ω. Next, we used the UAS pixel NDVI values to fit the downscaled model parameters:

$$\widehat{\beta} = (Q^T Q)^{-1} Q^T \mathbf{u}, \tag{3.2}$$

where $\widehat{\beta} = [\widehat{\beta}_0 \;\; \widehat{\beta}_1]^T$ are the regression model parameter estimates, $Q = [\mathbf{1} \;\; \mathbf{q}]$ is the predictor matrix, $\mathbf{1}$ is a vector that has all elements of 1, $\mathbf{q}$ is the vector of all Sentinel pixel NDVI values from the observed sites, and $\mathbf{u}$ is the vector of UAS pixel NDVI values from the observed sites used to fit the statistical downscaling regression model (i.e., $u(s)$ serves as a proxy for $m(s)$). The parameter estimates were used to create fitted values $\widehat{m}(s)$, given by:

$$\widehat{m}(s) = \widehat{\beta}_0 + \widehat{\beta}_1 \cdot q(s). \tag{3.3}$$

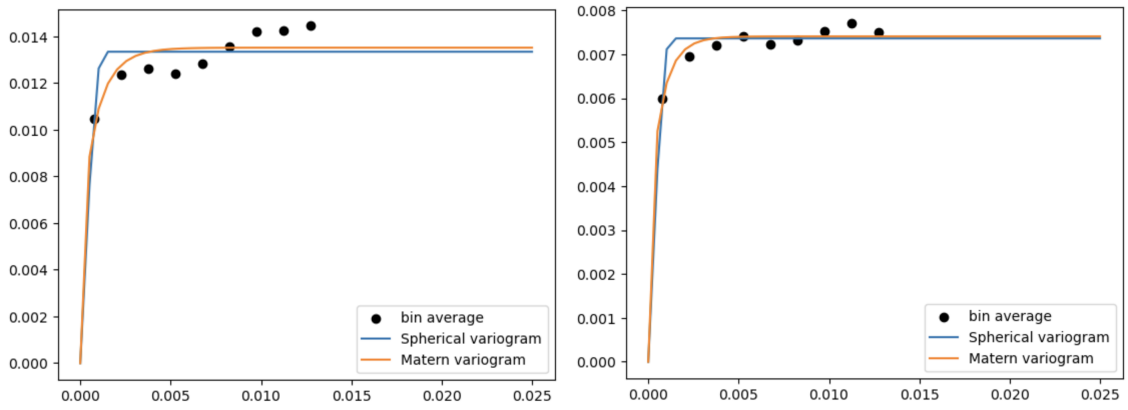

(a) Upper Field (b) Lower Field

Figure 3.2: Sample variograms with the fitted lines for Spherical and Matérn variogram models.

From this point, we calculated the regression residuals $e(s) = u(s) - \widehat{m}(s)$ and formed the sample variogram by binning the residual values, as in Chapter 2. We fit Spherical and Matérn variogram models (Equations 2.13 and 2.14) to the sample variograms for both the upper field and lower field, with the Matérn models providing a better fit by adapting to the curvature of the binned residuals for both fields (Figure 3.2). The resulting variogram parameter estimates are provided in Table 3.1 (all nuggets are set to zero, and smoothness parameter $\nu = 0.2$ for both Matérn variograms).

Table 3.1: Variogram parameter estimates for the upper and lower field models.

Variogram	**Sill**	**Range**
Spherical - Upper Field	0.0133	0.00127
Matérn - Upper Field	0.0135	0.00053
Spherical - Lower Field	0.00736	0.00121
Matérn - Lower Field	0.00741	0.000414

After forming the spatial correlation model, we fit our RK model using OLS regression and the estimates of the spatial variogram to account for the spatial autocorrelation during the fitting process.

The fitted RK model then creates our RK predictions (Equation 2.12):

$$\hat{z}(s) = \widehat{m}(s) + \hat{e}(s) = \widehat{\beta}_0 + \widehat{\beta}_1 \cdot q(s) + \sum_{i=1}^{n} \lambda_i \cdot e(s_i), \tag{3.4}$$

where $\hat{e}(s)$ is the interpolated residual component; λ_i are the kriging weights determined by the spatial correlation structure of the residuals; and $e(s_i)$ are the residuals of the observed data $u(s_1), \ldots, u(s_i), \ldots, u(s_n)$ at sample sites $s_1, \ldots, s_i, \ldots, s_n$. With the fitted model in hand, this process concluded by using the Sentinel pixel polygons to isolate a single 100x100 UAS pixel-sized section of the field, plugging the downsampled Sentinel pixel NDVI values and spatial coordinates for each pixel in the isolated area into the fitted RK model, producing the RK model predictions for each pixel in the isolated area, and repeating these steps on each 100x100 UAS pixel-sized area in the field. The result of this procedure was a raster of the upper and lower fields populated with all of the RK predictions of downscaled Sentinel pixel values (Figure 3.3).

3.2 Artificial Augmentation

Two additional predictors were formed from the artificial augmentation algorithm introduced in Section 2.2 (Equations 2.17-2.20). The first such predictor takes UAS NDVI values as the weighting factor of a Sentinel pixel NDVI value. In order to proliferate a spatial variety of UAS resolution pixel values within a single Sentinel pixel, our AA algorithm uses the ratio of a single UAS NDVI value to the average NDVI value of all UAS pixels within the Sentinel pixel to weight the Sentinel NDVI value and assigns the weighted value to the single UAS pixel. A workflow of the AA reweighting algorithm procedures is provided in Table 3.2. This process was repeated for all UAS pixels within a Sentinel pixel, and for all Sentinel pixels

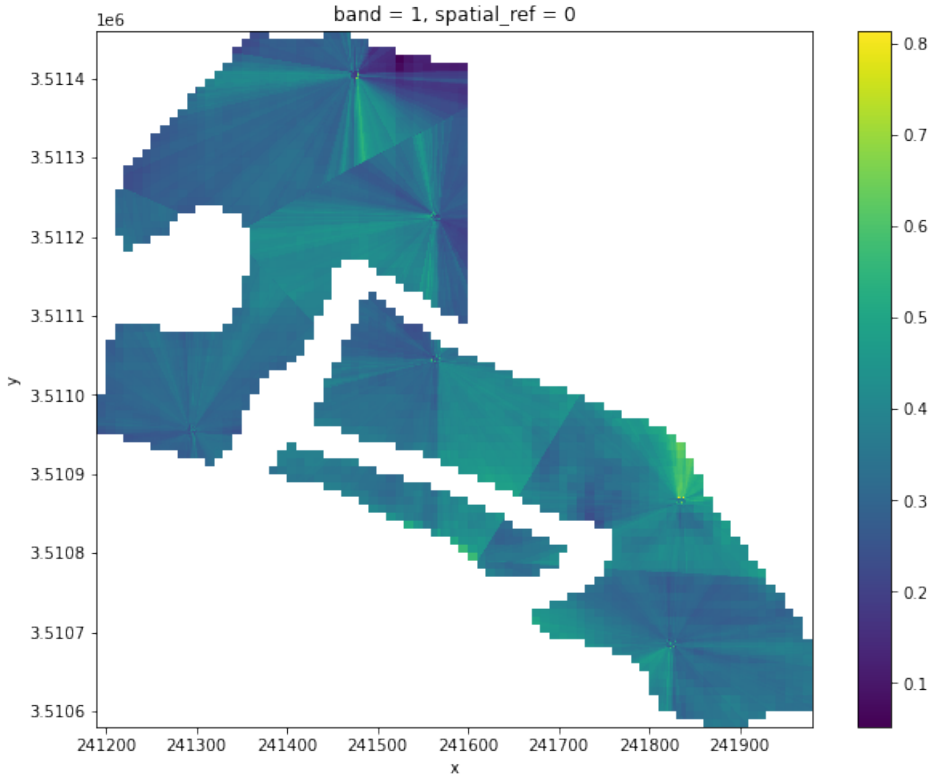

Figure 3.3: The regression kriging predictor possesses a starburst visual effect as the predictions were extrapolated from the sampling plots

across our study area remaining after the filtering process detailed in Section 3.1. Once all Sentinel pixels underwent the AA reweighting process, an OLS regression downscaled the reweighted Sentinel pixel values to the UAS level. To create the second such predictor, we reweighted the RK predictions using the AA algorithm to reintroduce the predictions to the spatial variation found in the UAS pixels (Equation 2.21). We calculated the average RK prediction value within a single Sentinel pixel boundary, used the ratio of a single UAS NDVI value to the average NDVI value of all UAS pixels within the Sentinel pixel to weight the RK prediction average value, and assigned the weighted value to the single UAS pixel.

Table 3.2: Workflow of the artificial augmentation reweighting process applied to UAS and Sentinel NDVI values.

Procedure	Formula
Step 1: Average all UAS pixel NDVI values within one Sentinel pixel	Average UAS NDVI = Sum of UAS pixel NDVI values / number of UAS pixels within Sentinel pixel
Step 2: Calculate the weight coefficient	Weight = UAS pixel NDVI value / Average UAS NDVI
Step 3: Assign weighted Sentinel NDVI value to each UAS pixel	Weighted Sentinel NDVI = Weight * Sentinel pixel NDVI value

Finally, we created a fourth predictor by taking the average of the RK, AA, and RKAA predictors (Equation 2.22). As noted in Chapter 2, the joint predictor lags behind the AA and RKAA predictors in performance due to the inclusion of the standard RK predictor. As the RK predictor's performance improves, so too shall the joint predictor. The four predictors following the downscaling procedures are depicted in Figure 3.4. Although the figures in panels b-d appear to show some crop row alignment, the diagonal lines shown are not actually the crop rows; this appears to be a Python plotting or image rendering quirk with the program deciding which pixels to show when the image resolution is finer than the plot/rendering. As mentioned in Chapter 2, the predictors using the AA algorithm do not spatially extrapolate values from the sampled sites using kriging; therefore, these plots do not show a starburst effect as seen in the RK predictor in panel a. The MSE and bias values for the four downscaled predictors, given in Table 3.3, were calculated by taking the difference between the UAS NDVI and downscaled NDVI values at every UAS pixel across the entire study site. These measures show similar trends to the simulation data in Section 2.3.2. Namely, the RK and RKAA predictors show the highest error, while the satellite AA predictor shows the lowest error, and the joint predictor averages out the results of the other three. Although these predictors each generate very little bias, all four predictors underestimated

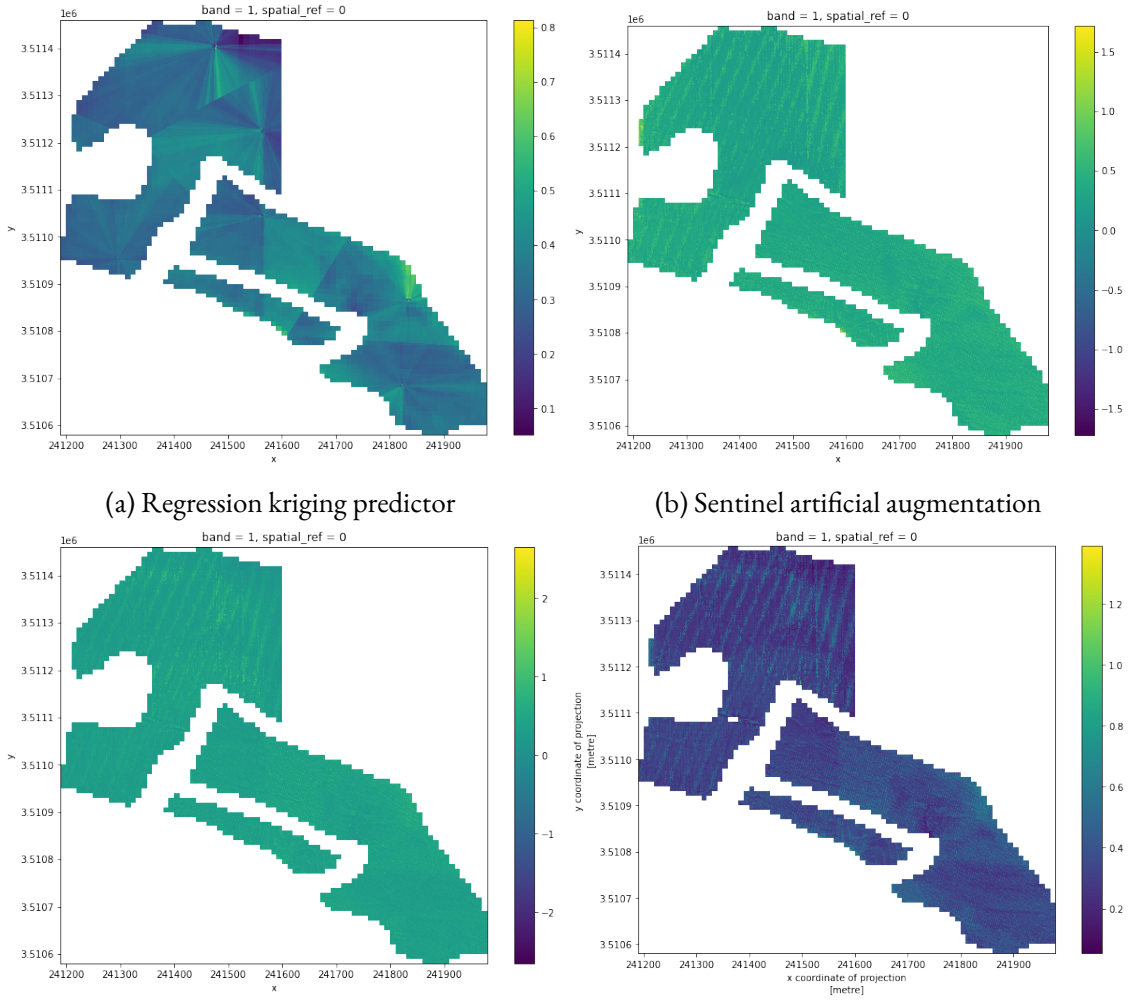

(a) Regression kriging predictor

(b) Sentinel artificial augmentation

(c) Artificial augmentation applied to regression kriging predictor

(d) Joint predictor

Figure 3.4: Four statistical downscaling predictors formed from Sentinel and UAS NDVI values.

downscaled NDVI when compared to the UAS imagery, potentially a symptom of the reduced satellite NDVI illustrated in Figure 1.19. We see that the joint predictor dampens the worst of the biases, as intended.

Table 3.3: Mean squared error and bias statistics from four downscaled predictors measured against the UAS imagery.

Predictor	**MSE**	**Bias**
Regression kriging	0.02371	-0.00840
Satellite artificial augmentation	0.00394	-0.00721
Regression kriging artificial augmentation	0.01255	-0.00840
Joint predictor	0.00900	-0.00800

3.3 Biomass Predictions

Above ground biomass measurements were only available for six sampling plots throughout the cotton fields. Therefore, we utilized the AA algorithm and workflow given in Section 2.2 to produce biomass values for each UAS pixel within the biomass sampling plot area (Equation 2.23). This process takes the summary biomass measurement for each 30 m by 10 crop row plot and converts that quantity into a raster of biomass per pixel weighted by the UAS NDVI value at each pixel.

We used a separate OLS regression for each predictor to model biomass. Each OLS model takes the predictor values as the only explanatory variable in order to make biomass predictions (Equations 2.24-2.27). The biomass predictions (in g/pixel) for the four different predictors across the entire study site, as well as the predictions formed from the original UAS NDVI pixel values:

$$\hat{b}(s) = \widehat{\beta}_0 + \widehat{\beta}_1 \cdot u(s), \tag{3.5}$$

are displayed in Figure 3.5. The UAS pixels are the closest remotely sensed imagery to the ground level, which allows them to serve as an "ideal" predictor. The different MSE values produced by the five biomass

predictions are highlighted in Table 3.4. These MSE calculations took the difference between the observed and predicted values at every UAS pixel with the six 30 m by 10 crop row plots where biomass measurements were taken. As expected, we see that all four predictors fall short of the measurements produced by the UAS level "ideal" predictor. The AA, RKAA, and joint predictors show roughly equal performance among our downscaled predictors, with about twice the error of the UAS predictor, while the standard RK predictor falls far behind the others based on accuracy.

Table 3.4: Mean squared error statistics from five biomass predictors.

Predictor	**MSE**
Regression kriging	0.00945
Satellite artificial augmentation	0.00165
Regression kriging artificial augmentation	0.00180
Joint predictor	0.00216
UAS level "ideal" predictor	0.00089

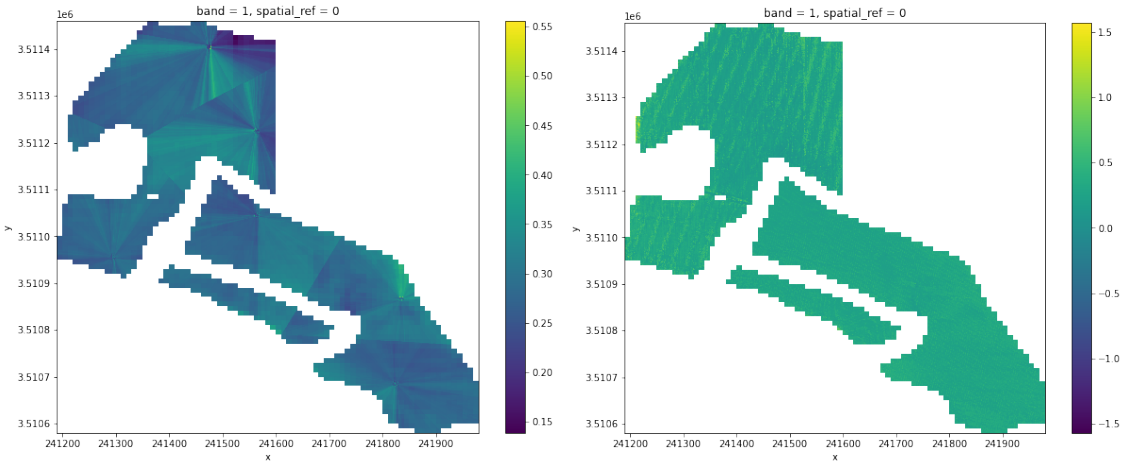

(a) Regression kriging predictor

(b) Sentinel artificial augmentation

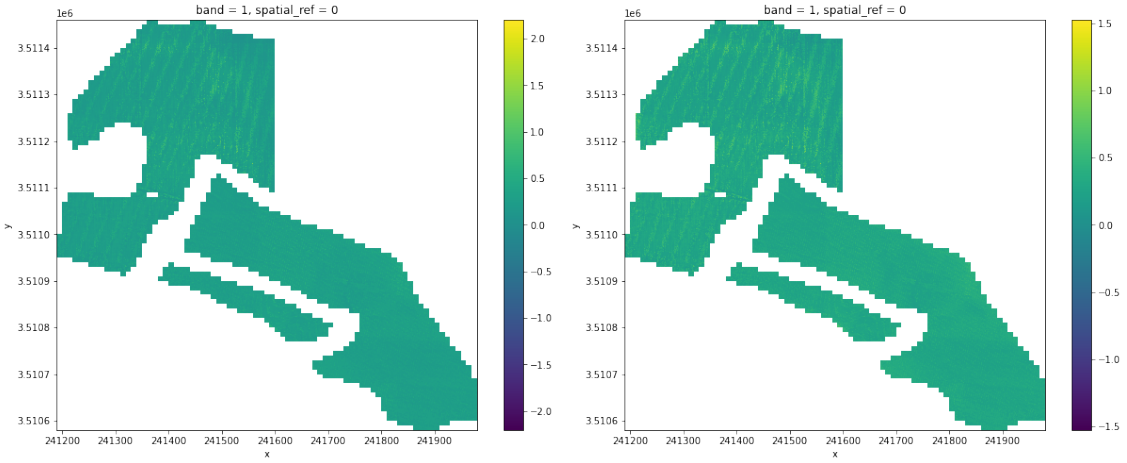

(c) Artificial augmentation applied to regression kriging predictor

(d) Joint predictor

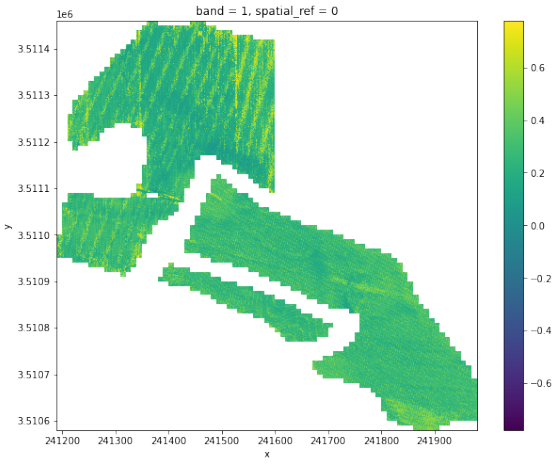

(e) UAS predictor

Figure 3.5: Biomass prediction plots (in g/pixel) from the five predictors.

Chapter 4

Conclusion and Future Directions

The LTAR Network seeks to build a strong understanding of the agricultural regions of similarity within the GACP LTAR site. To understand the region as a whole, we must take steps to first understand crop behavior within a single farm. This study highlights the connection between remote sensing multispectral imagery and ground level biomass.

Small fields (i.e., < 5 ha) are prevalent within the GACP LTAR site. These types of fields cannot be analyzed properly with only moderate-scale satellite imagery. Our multiscale research is of particular importance to the regionalization efforts of LTAR researchers studying fields in the GACP and areas like this because of the addition of the fine-scale UAS remotely sensed imagery to provide sub-satellite-pixel variation that more closely represents the ground level vegetation.

By exploring the surface distribution of biomass through spatial models, we propose new multiscale methods to produce biomass predictions based on downscaled remotely sensed multispectral imagery and ground level biomass. This approach utilizes the intermediate level of the UAS imagery to study sub-satellite-pixel variation, which improves the connection between the satellite imagery and the surface.

While statistical downscaling approaches typically make predictions at a discrete number of ground surface points, we propose adaptations of these methods to construct a grid of predictions by treating each UAS pixel as a spatial site. We form two novel sets of statistical downscaling predictions by combining the RK and AA procedures to form the RKAA and Joint predictors.

Many avenues of future research exist to further the scope of this study, including:

2018 Growing Season: The UAS drone flights and ground level above ground biomass were collected for the entirety of the 2018 growing season. This study focuses solely on the earliest sampling/acquisition date of imagery and ground level data (above ground biomass and UAS imagery from June 18 and Sentinel imagery from June 11). A future study might extend this methodology to additional dates. Further, additional studies might consider methods to examine the temporal effects of above ground biomass development, linking the sampling dates together through time series models. In addition, the temporal lag between the increase in NDVI and the increase in biomass depicted in Figure 1.18 can be fully explored. Following this first study, there is potential for our research to show a consistent spatial biomass pattern throughout the growing season. Having a consistent spatial pattern of growth reduces the number of UAS flights necessary for understanding the surface spatial distribution of biomass and allows researchers to downscale satellite imagery more frequently.

Machine Learning Models: As a first study into this mixture of agricultural crops and remote sensing data, we employ simple linear regressions to connect the data layers and construct our biomass predictions. Future studies might choose to implement and compare more sophisticated machine learning and deep learning models, such as LASSO and ridge regressions, support vector regressions, random forest regressions, and convolutional neural networks, to perform the downscaling tasks and to form biomass predictions.

Vegetation Indices: As with the expanded machine learning model options, this analysis can be further extended by introducing additional vegetation indices into the models. As a first study, we focus solely on NDVI for its overall quantification of plant greenness and health. Future studies might choose to study the relationships that exist between biomass and other vegetation indices, such as SAVI and EVI2. Further, future studies might consider a combination of vegetation indices based on the plant phenology (i.e., using a different vegetation index for each sampling date) to maximize the predictive power of the model across various time points in the growing season.

Ground Level Covariates: Our study does not consider any ground level covariates in the biomass prediction models. These covariates have the potential to explain in greater detail the spatial pattern of biomass. Examples of potential ground level covariates include elevation, precipitation, soil type, and soil moisture.

Multiple Crop Classes: This study considers only cotton crops when predicting biomass. Future studies might seek to apply this methodology to other crop classes, such as peanuts, corn, and soybeans. Additionally, a pixel classification model may be utilized when studying the sampling dates early in the growing season to separate out the pixels that mostly contain soil (i.e., no plant growth). This classification routine might enhance model accuracy by preventing the overprediction of biomass at pixel locations where no plant growth is present.

Other Remote Sensing Imagery: Our study performs statistical downscaling of Sentinel-2 imagery to enhance the satellite resolution to that of the UAS imagery. This approach can be extended to other remote sensing data sources, such as Landsat 8 OLI imagery. In fact, we initially intended to run our statistical downscaling model on the Landsat 8 imagery, but the large number of UAS pixels within each Landsat pixel made our methodology computationally infeasible. Future studies might investigate computation-

friendly adjustments to the methodology in this study, while also seeking out high-performance computing resources. Conversely, future studies might also consider the effect of aggregating UAS imagery to a coarser resolution. Regardless of the imagery sources utilized, we recommend that biomass sampling and the UAS flight coincide on at least one date per year with the other remote sensing imagery in order to synchronize the various sensors.

Cloud Cover: During our exploratory data analysis, we were forced to exclude several satellite images due to poor visibility caused by cloud cover. One future direction we suggest is a study on methods to mitigate the effects of cloud cover in order to preserve images as viable data for analysis (e.g., multifrequency Synthetic Aperture Radar (SAR) plus optical imagery; Dingle Robertson et al., 2020). UAS images are less affected by cloud cover because the sensor is not flown high enough to include cloud blockages. We document the connection between the satellite and UAS imagery in our study. Therefore, we propose utilizing this connection to fill in the pixels blocked by clouds. This approach treats the pixels blocked by clouds as missing data and fills in the values using the unaffected UAS pixels as a guide. A similar approach can be taken with correcting ground discoloration caused by cloud shadows. For some satellite images, the cloud cover may be too significant to warrant such a correction. In this case, we recommend an interpolation between the two satellite images immediately prior to and following the compromised image, as long as those images are unaffected by cloud cover, or a synthetic data fusion approach (Gao et al., 2006).

Kriging Enhancements: Three of our four proposed statistical downscaling models result from kriging. Under the current implementation, our kriging models suffered from a severe lack of spatially distributed data, with data confined to six concentrated sites. The high concentration of data causes the kriging models to underperform relative to the Sentinel-2 AA model. With the availability of more

spatially robust data in future studies, kriging remains a viable component in our statistical downscaling models. Jin et al. (2018) created a coarse-scale regression model to krige the residuals at the coarse level before making final predictions by adding the interpolated spatial correlation term to a fine-scale regression model. This approach might circumvent the starburst effect we observe in our current RK predictions. Additional studies might also consider the viability of an expectation-maximization (EM) algorithm to enhance the initial biomass predictions found here.

Bibliography

Abramowitz, M. and Stegun, I. (1964). *Handbook of Mathematical Functions with Formulas, Graphs, and Mathematical Tables*. United States Department of Commerce, National Bureau of Standards, Gaithersburg, Maryland.

AgEagle Aerial Systems Inc. (2024). RedEdge-P. https://ageagle.com/drone-sensors/rededge-p-high-res-multispectral-camera/ [Accessed: 2024-07-10].

Bean, A. R., Coffin, A. W., Arthur, D. K., Baffaut, C., Holifield Collins, C., Goslee, S. C., Ponce-Campos, G. E., Sclater, V. L., Strickland, T. C., and Yasarer, L. M. (2021). Regional frameworks for the USDA Long-Term Agroecosystem Research Network. *Frontiers in Sustainable Food Systems*, 4.

Biswas, A. and Si, B. C. (2013). Model averaging for semivariogram model parameters. In Grundas, S. and Stepniewski, A., editors, *Advances in Agrophysical Research*, chapter 4. IntechOpen, Rijeka.

Boser, B. E., Guyon, I. M., and Vapnik, V. N. (1992). A training algorithm for optimal margin classifiers. In *Proceedings of the 5th Annual Workshop on Computational Learning Theory*, pages 144–152. ACM.

Coffin, A., Cosh, M., and Pisarello, K. (2023). Data from: Two years of cotton (*Gossypium hirsutum L.*) data from the Gulf Atlantic Coastal Plain LTAR Network site. *Ag Data Commons, National Agricultural Library*.

Coffin, A., Cosh, M., and Pisarello, K. (2024). Two years of cotton (*Gossypium hirsutum L.*) data from the Gulf Atlantic Coastal Plain LTAR Network site. *Scientific Data*. In review.

Coffin, A. W., Bosch, D. D., Strickland, T. C., Endale, D. M., Pisani, O., and Lowrance, R. (2022). Cropping patterns over two decades in the Little River Experimental Watershed, Georgia, USA. In *Proceedings of the Seventh Interagency Conference on Research in the Watersheds*, pages 186–190. U.S. Department of Agriculture Forest Service, Southern Research Station.

Cressie, N. A. C. (1993). *Statistics for Spatial Data*. Wiley Series in Probability and Mathematical Statistics. John Wiley and Sons, Inc., 111 River Street, Hoboken, NJ 07030.

Dingle Robertson, L., Davidson, A. M., McNairn, H., Hosseini, M., Mitchell, S., de Abelleyra, D., Verón, S., le Maire, G., Planells, M., Valero, S., Ahmadian, N., Coffin, A., Bosch, D., Cosh, M. H., Basso, B., and Saliendra, N. (2020). C-band Synthetic Aperture Radar (SAR) imagery for the classification of diverse cropping systems. *International Journal of Remote Sensing*, 41(24):9628–9649.

Dong, J., Zhuang, D., Huang, Y., and Fu, J. (2009). Advances in multi-sensor data fusion: Algorithms and applications. *Sensors*, 9:7771–7784.

Farabet, C., Couprie, C., Najman, L., and LeCun, Y. (2013). Learning hierarchical features for scene labeling. *IEEE Transactions on Pattern Analysis and Machine Intelligence*, 35(8):1915–1929.

Gahrouei, O. R., McNairn, H., Hosseini, M., and Homayouni, S. (2020). Estimation of crop biomass and leaf area index from multitemporal and multispectral imagery using machine learning approaches. *Canadian Journal of Remote Sensing*, 46(1):84–99.

Gao, F., Anderson, M. C., Zhang, X., Yang, Z., Alfieri, J. G., Kustas, W. P., Mueller, R., Johnson, D. M., and Prueger, J. H. (2017). Toward mapping crop progress at field scales through fusion of Landsat and MODIS imagery. *Remote Sensing of Environment*, 188:9–25.

Gao, F., Masek, J., Schwaller, M., and Hall, F. (2006). On the blending of the Landsat and MODIS surface reflectance: Predicting daily Landsat surface reflectance. *IEEE Transactions on Geoscience and Remote Sensing*, 44(8):2207–2218.

Goovaerts, P. (1997). *Geostatistics for Natural Resources Evaluation*. Oxford University Press, New York.

Gorelick, N., Hancher, M., Dixon, M., Ilyushchenko, S., Thau, D., and Moore, R. (2017). Google earth engine: Planetary-scale geospatial analysis for everyone. *Remote Sensing of Environment*.

Gotway, C. A. and Young, L. J. (2002). Combining incompatible spatial data. *Journal of the American Statistical Association*, 97(458):632–648.

Gotway, C. A. and Young, L. J. (2007). A geostatistical approach to linking geographically aggregated data from different sources. *Journal of Computational and Graphical Statistics*, 16(1):115–135.

Guo, B., Gunn, S. R., Damper, R. I., and Nelson, J. D. B. (2008). Customizing kernel functions for SVM-based hyperspectral image classification. *IEEE Transactions on Image Processing*, 17(4):622–629.

Guo, Y., Jia, X., and Paull, D. (2018). Effective sequential classifier training for SVM-based multitemporal remote sensing image classification. *IEEE Transactions on Image Processing*, 27(6):3036–3048.

Hamdi, Z. M., Brandmeier, M., and Straub, C. (2019). Forest damage assessment using deep learning on high resolution remote sensing data. *Remote Sensing*, 11(17):1976.

Hengl, T. (2009). *A Practical Guide to Geostatistical Mapping*, volume 2 of *Scientific and Technical Research*. Office for Official Publications of the European Communities, Luxembourg.

Hengl, T., Heuvelink, G. B., and Rossiter, D. G. (2007). About regression-kriging: From equations to case studies. *Computers & Geosciences*, 33(10):1301–1315.

Hengl, T., Heuvelink, G. B., and Stein, A. (2004). A generic framework for spatial prediction of soil variables based on regression-kriging. *Geoderma*, 120(1-2):75–93.

Heute, A. R. (1988). A soil-adjusted vegetation index (SAVI). *Remote Sensing of Environment*, 25(3):295–309.

Isaaks, E. H. and Srivastava, R. M. (1989). *Applied Geostatistics*. Oxford University Press, New York.

Jensen, J. R. (2000). *Remote Sensing of the Environment: An Earth Resource Perspective*. Prentice Hall, New Jersey.

Jeong, D., St-Hilaire, A., Ouarda, T., and Gachon, P. (2012a). A multivariate multi-site statistical downscaling model for daily maximum and minimum temperatures. *Climate Research*, 54(2):129–148.

Jeong, D., St-Hilaire, A., Ouarda, T., and Gachon, P. (2012b). Multisite statistical downscaling model for daily precipitation combined by multivariate multiple linear regression and stochastic weather generator. *Climatic Change*, 114:567–591.

Jin, Y., Ge, Y., Wang, J., Heuvelink, G. B., and Wang, L. (2018). Geographically weighted area-to-point regression kriging for spatial downscaling in remote sensing. *Remote Sensing*, 10(4):579–600.

Kornelsen, K. C., Cosh, M. H., and Coulibaly, P. (2015). Potential of bias correction for downscaling passive microwave and soil moisture data. *Journal of Geophysical Research: Atmospheres*, 120(13):6460–6479.

Kumar, J., Coffin, A. W., Baffaut, C., Ponce-Campos, G. E., Witthaus, L., and Hargrove, W. W. (2023). Quantitative representativeness and constituency of the Long-Term Agroecoststem Research Network and analysis of complementarity with existing ecological networks. *Environmental Management*, 72:705–726.

Kussul, N., Lavreniuk, M., Skakun, S., and Shelestov, A. (2017). Deep learning classification of land cover and crop types using remote sensing data. *IEEE Geoscience and Remote Sensing Letters*, 14(5):778–782.

LeCun, Y., Bengio, Y., and Hinton, G. (2015). Deep learning. *Nature*, 521:436–444.

Liew, S. (2001). Centre for Remote Imaging, Sensing and Processing (CRISP). www.crisp.nus.edu.sg [Accessed: 2023-07-04].

Markham, K., Frazier, A. E., Singh, K. K., and Madden, M. (2022). A review of methods for scaling remotely sensed data for spatial pattern analysis. *Landscape Ecology*, 38:619–635.

Matheron, G. (1963). Principles of geostatistics. *Economic Geology*, 58(8):1246–1266.

Matheron, G. (1969). Le krigeage universel. *École nationale supérieure des mines de Paris.*, Part 1 of Cahiers du Centre de morphologie mathématique de Fontainebleau.

Meng, Q., Liu, Z., and Borders, B. E. (2013). Spatial extrapolation: The science of predicting ecological patterns and processes. *Cartography and Geographic Information Science*, 40(1):28–39.

Miller, J. R., Turner, M. G., Smithwick, E. A., Dent, L., and Stanley, E. H. (2004). Spatial extrapolation: The science of predicting ecological patterns and processes. *BioScience*, 54(4):310–320.

Mukherjee, S., Joshi, P. K., and Garg, R. D. (2015). Regression-kriging technique to downscale satellite-derived land surface temperature in heterogeneous agricultural landscape. *IEEE Journal of Selected Topics in Applied Earth Observations and Remote Sensing*, 8(3):1245–1250.

Njuki, S. M., Mannaerts, C. M., and Su, Z. (2020). An improved approach for downscaling coarse-resolution thermal data by minimizing the spatial averaging biases in random forest. *Remote Sensing*, 12(21):3507–3529.

Odeh, I. O. A., McBratney, A. B., and Chittleborough, D. J. (1995). Further results on prediction of soil properties from terrain attributes: heterotopic cokriging and regression-kriging. *Geoderma*, 67(3-4):215–226.

Pal, M. (2009). Kernel methods in remote sensing: A review. *ISH Journal of Hydraulic Engineering*, 15(1):194–215.

Pan, X., Yang, Y., Cao, C., Zhang, X., and Shan, L. (2018). Applicability of downscaling land surface temperature by using normalized difference sand index. *Scientific Reports*, 8(1):9530–9543.

Pan Geography (2022). Pan Geography. https://pangeography.com/ [Accessed: 2023-07-04].

Powell, J., Stone, A., Coffin, A., Madden, M., Seymour, L., Ahn, J., and Holder, M. (2022). Using remote sensing and deep learning to assess regional boundaries of the Gulf Atlantic Coastal Plain long-term

agroecosystem research network site. In *Proceedings of the Seventh Interagency Conference on Research in the Watersheds*, pages 195–198. U.S. Department of Agriculture Forest Service, Southern Research Station.

Revill, A., Florence, A., MacArthur, A., Hoad, S., Rees, R., and Williams, M. (2020). Quantifying uncertainty and bridging the scaling gap in the retrieval of leaf area index by coupling Sentinel-2 and UAV observations. *Remote Sensing*, 12(11):1843.

Richert, W. and Coelho, L. P. (2013). *Building Machine Learning Systems with Python*. PACKT Publishing.

Scott, G. J., England, M. R., Starms, W. A., Marcum, R. A., and Davis, C. H. (2017). Training deep convolutional neural networks for land-cover classification of high-resolution imagery. *IEEE Geoscience and Remote Sensing Letters*, 14(4):549–553.

Sohn, G. and Dowman, I. (2007). Data fusion of high-resolution satellite imagery and lidar data for automatic building extraction. *ISPRS Journal of Photogrammetry & Remote Sensing*, 62:43–63.

Stone, A. (2023). A methodology for scaling agricultural biomass from ground to regional scales using remote sensing and machine learning analysis.

Tucker, C. J. (1978). A comparison of satellite sensor bands for vegetation monitoring. *Photogrammetric Engineering and Remote Sensing*, 44(11):1369–1380.

Tuo, R. and Wang, W. (2020). Kriging prediction with isotropic Matérn correlations: Robustness and experimental designs. *Journal of Machine Learning Research*, 21(187):1–38.

USDA-ARS (2022). Long-Term Agroecosystem Research (LTAR) Network. https://ltar.ars.usda.gov/ [Accessed: 2023-07-04].

USDA-ARS (2024). Southeast Watershed Research Laboratory. https://www.ars.usda.gov/southeast-area/tifton-ga/southeast-watershed-research[Accessed: 2024-07-11].

USGS EROS (2019). USGS EROS Archive - Sentinel-2 - Comparison of Sentinel-2 and Landsat. https://www.usgs.gov/centers/eros/science/usgs-eros-archive-sentinel-2-comparison-sentinel-2-and-landsat [Accessed: 2023-07-04].

Wang, W., Tuo, R., and Wu, C. J. (2019). On prediction properties of kriging: Uniform error bounds and robustness. *Journal of the American Statistical Association*, 115(530):920–930.

Washington, B. J. (2020). *An Adapted VAR-EM Imputation of Climate Data and Statistical Downscaling of Temperature, Precipitation, and Solar Radiation in Puerto Rico*. PhD thesis, University of Georgia, Athens, GA.

Wikipedia (2024). Variogram. https://en.wikipedia.org/wiki/Variogram[Accessed: 2024-06-03].

Yin, G., Li, A., Wu, C., Wang, J., Xie, Q., Zhang, Z., Nan, X., Jin, H., Bian, J., and Lei, G. (2018). Seamless upscaling of the field-measured grassland aboveground biomass based on Gaussian process regression and gap-filled Landsat 8 OLI reflectance. *International Journal of Geo-Information*, 7(7):242.

Zappa, L., Forkel, M., Xaver, A., and Dorigo, W. (2019). Deriving field scale soil moisture from satellite observations and ground measurements in a hilly agricultural region. *Remote Sensing*, 11(22):2596.

Zhang, J. (2010). Multi-source remote sensing data fusion: status and trends. *International Journal of Image and Data Fusion*, 1(1):5–24.

Zhang, Y., Yang, W., Sun, Y., Chang, C., Yu, J., and Zhang, W. (2021). Fusion of multispectral aerial imagery and vegetation indices for machine learning-based ground classification. *Remote Sensing*, 13(8):1411.

Appendix A

When testing our methodology through simulations, we ran into an issue with one of the simulations. The computer processing failed due to the variogram fitting process timing out. This seems to have occurred because the sample variogram (Figure A.1) shows an upward trend and does not reach a sill. Variogram models expect to come across the sample variogram sill in order to fit their tuning parameters properly. A sample variogram without a sill prevents the variogram models from fitting. Additionally, a sample variogram without a sill may indicate a lingering trend that hasn't been removed, or even long range dependence in the data. Based on the plots of ϵ, the UAS data, and the ground level data (Figures A.2 and A.3; from Equations 2.29 and 2.30), with the lower triangular section containing mostly high values and the upper triangular section containing mostly low values, some long range dependence could be present in this iteration of the simulation. The seeds used to create these spatial random fields are X_1: 5150895; X_2: 1878608; and ϵ: 2053352.

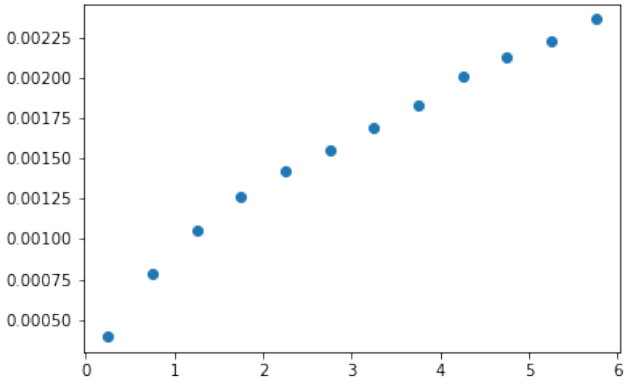

Figure A.1: Sample variogram from the failed seed.

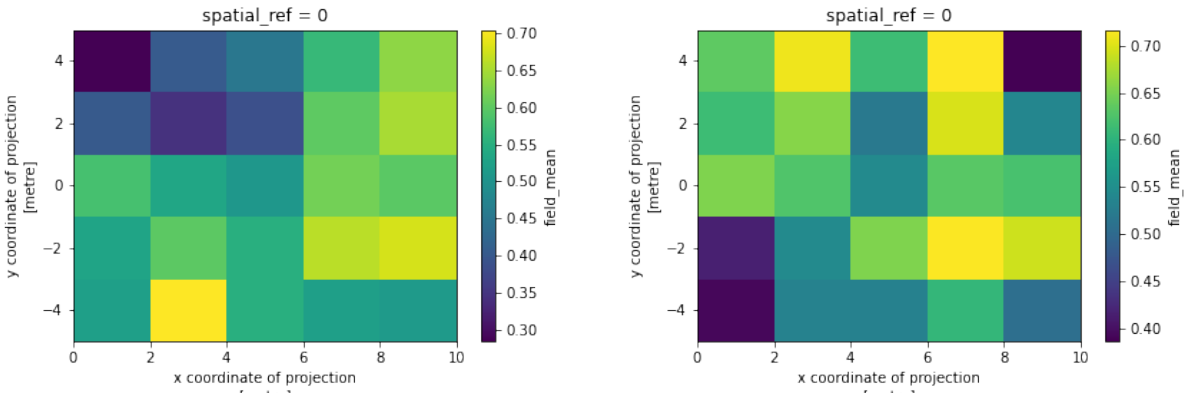

(a) X_1 (b) X_2

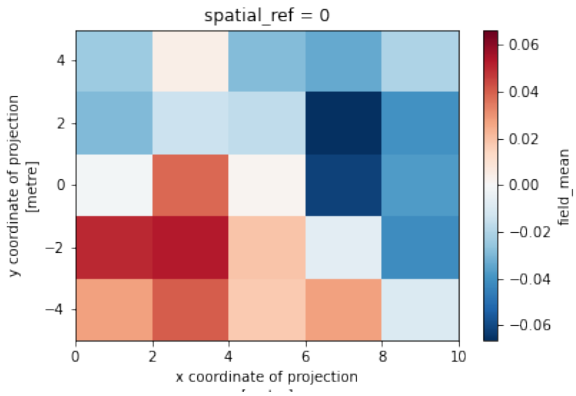

(c) ϵ

Figure A.2: Simulated X_1, X_2, and ϵ from the failed seed.

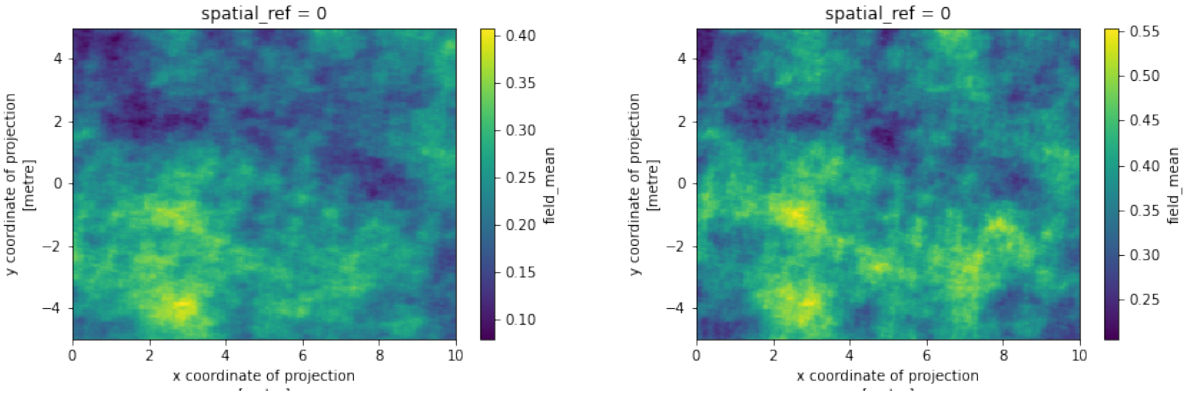

(a) UAS level

(b) Ground level

Figure A.3: Simulated UAS level and ground level response variables from the failed seed.